Design, Implementation and First Results of the ANITA-HiCal Experiment

By

Jessica G Stockham

Submitted to the Department of Physics and Astronomy and the
Graduate Faculty of the University of Kansas
in partial fulfillment of the requirements for the degree of
Doctor of Philosophy

Committee members

David Z. Besson, Chairperson

Christopher Allen

Hume Feldman

Ian Lewis

Hui Zhao

Date defended: 11 May 2018

The Thesis Committee for Jessica G Stockham certifies
that this is the approved version of the following thesis :

Design, Implementation and First Results of the ANITA-HiCal Experiment

David Z. Besson, Chairperson

Date approved: 11 Dec 2018

Abstract

The ANITA (ANtarctic Impulsive Transient Antenna) experiment is a balloon-borne suite of radio frequency antennas deployed during the austral summers in 2006, 2011, 2014, and 2016 to travel on the circumpolar winds over the ice sheets of Antarctica. The goal of the ANITA experiment is to detect UHE (Ultra-High Energy) neutrinos (10^9 to 10^{13} GeV) and cosmic rays through the RF (Radio-Frequency) emission of in-ice and atmospheric particle showers initiated, respectively, by these two types of particles. Radio detection of ultra-high energy cosmic ray (UHECR) extensive air showers (EAS) above the Antarctic continent has been demonstrated by the four flights of the ANITA experiment. The majority of the detected events were received as reflections from the ice surface. In order to reconstruct the energy of these reflected events, it is necessary to quantify any decoherence in the ANITA frequency band (180-1200 MHz) due to roughness of the ice surface. The purpose of this work is to provide details on the HiCal (High-altitude Calibration) experiment implemented to measure surface reflectivities of the Antarctic ice as a part of the ANITA experiment. The first HiCal payload flew in conjunction with the ANITA-3 flight in 2014 and provided a set of direct and reflected event pairs from which an inclination angle dependent measurement of the surface reflection coefficients was determined. It was found that at the highest incidence angles (most skimming) this coefficient deviates significantly both from the Fresnel predicted coefficients and from the model derived coefficients currently used in the ANITA analysis reconstruction of UHECR events.

Acknowledgements

I would like to thank my adviser Dave for giving me the opportunity, resources, and guidance to complete this work, my husband Mark for being my desk buddy and roof buddy and travel-halfway-around-the-world buddy, my parents for always supporting my endeavors and encouraging me to question and reason, all my family and friends for their interest and continued support, and my babies, Rolo and Maggie, for showing me a whole new world that I'm grateful for every day.

Contents

List of Figures

Chapter 1

Overview

This work is organized in a manner to provide details on the topics most relevant to understanding the purpose, design, performance, and analysis of the HiCal experiment. This chapter serves as a brief, top-down outline for the physical processes of interest and how the ANITA and HiCal experiments fit into the study of said processes.

1.1 The Big Picture

Throughout the history of the universe, physical processes have acted to convert matter and energy into other forms of matter and energy. The composition of the universe and of objects in the it are vital keys to understanding how it has evolved and in determining the fundamental processes occurring in these conversions. Man-made particle accelerators have been used to produce proton-proton collisions up to 14 TeV but higher energy interactions can only be studied by observing the light and particle emissions from objects at the highest redshifts (most distant) and closer more energetic objects. These emissions, when they arrive at earth, are commonly referred to as cosmic rays (CR), a term coined by Victor Hess in 1912 [1]. Many different particles fall under the umbrella of CR including electrons, positrons [2], protons, heavier nuclei, and gamma rays.

Above a certain energy, the cosmic ray flux will be strongly attenuated due to interactions with the cosmic photon backgrounds. This limits the distance from source at which the ultra-high energy

(UHE) CR can be observed [3]. One of the products of these attenuation interactions is neutrinos. Neutrinos are very weakly attenuated by the cosmic photon backgrounds and furthermore, unlike cosmic rays, are neutral particles and will point back to their source location. Since the energy spectrum of these cosmogenic neutrinos is dependent on source composition, source evolution and initial energy of the UHECR [4], detecting these neutrinos and measuring their energy-flux spectrum will put constraints on the parameter space of the characteristics of these UHECR sources [5][6][7]. Cosmogenic neutrinos may also be produced directly by the same sources producing the UHECR. In both cases, detection of extra-galactic neutrinos will probe the high energy universe and determination of the energy-flux spectrum will provide measurements of the fundamental particle interactions which produced them. The interest in understanding the high energy universe and the potential for using these high energy particles as probes has spurred the development of an ever increasing number of experiments aiming to detect them. Aiding in this effort has been the maturation of the radio detection method, made possible by electromagnetic (EM) emissions in the radio frequency range from particle showers produced when the high energy particles interact with terrestrial and atmospheric nuclei. Cosmic rays will shower in the atmosphere while neutrinos, due to their longer interaction lengths, require a denser media to interact and produce showers. Large bodies of ice [8][9][10], salt [11][12][13], and sand [14] would serve as the most ideal detection volumes due to their dielectric properties and relative homogeneity.

1.2 The ANITA Experiment

One experiment that employs the radio-frequency emission detection method is the ANtarctic Impulsive Transient Antenna (ANITA). ANITA is an array of radio antennas operating in the frequency range of 200-1200 MHz. The array is part of a payload carried by high altitude balloons on circumpolar trajectories above the Antarctic continent. At its conception in the early 2000s, the main science goal for ANITA was detection of neutrinos with energy over 10^{18} eV in order to verify the energy of the Greisen-Zatsepin-Kuzmin (GZK) cutoff and to associate UHE neutrinos

with high energy acceleration sources, such as Active Galactic Nuclei (AGN) [15]. ANITA has conducted five flights over the Antarctic continent: a proof of concept flight in the 2003 austral season, [16], and full instrument flights in 2006 [17][18][19], 2008 [20][21], 2014 [22] and 2016 (analysis results pending). ANITA was initially devised to be a neutrino detector that would increase exposure to neutrino shower events by 1) being airborne to increase the surface area of ice being viewed at any given time, and 2) flying over the Antarctic ice-sheets which are fairly radio-transparent thus further increasing the detection volume. ANITA has not yet detected a neutrino event but has used the flight data to set limits on the cosmic neutrino flux. Though not its intended purpose, ANITA has proven capable of detecting the in-atmosphere showers produced by UHECR both directly and following reflections of the signals from the ice surface as well as thus far uncategorized upward going events [23][24]. Specifics about how ANITA detects and reconstructs the CR events are covered in Chapter 3.

1.3 The HiCal Experiment for ANITA Surface Reflection Calibration

While the Antarctic ice provides many benefits for detecting UHE particles, it is a naturally formed material with locational variation in temperature, composition and surface features which will have an effect on the propagation of radio waves. In order to accurately predict the expected detection rate for experiments and reconstruct the shower events, measurements of the ice bulk and surface properties is necessary. Measurements of the bulk properties and effects on RF propagation have been conducted in dedicated works [25][26][27] and as a part of the ANITA experiment itself via buried ground pulsers operated during the experiment flight.

Another step in reconstructing the UHECR events and any future detected neutrino events is accounting for surface effects on the reflection or transmission of the signals, specifically those that are location and frequency dependent as those properties will have the greatest impact on the reconstruction. Since the ice-sheets are a rough surface and surface roughness varies by geographic

location it is necessary to measure the reflection and transmission properties of the ice in the RF range of interest to reduce uncertainties in the reconstruction. Previous to this work, satellite and aircraft based surveys, modeling and simulations have been performed and are discussed in Chapter 4. However, only one of the satellite surveys overlapped the ANITA bandwidth and only the modeling done specifically for ANITA has covered the full bandwidth. The lab measurements taken over sand and aluminum foil in the 2-4 GHz range, also discussed in Chapter 4, are original to this work.

The High-altitude Calibration (HiCal) experiment is a partner experiment to ANITA designed specifically to create CR like pulses that are transmitted from altitudes of 35-40 km and will produce direct and reflected pairs of events received by ANITA. These event pairs can then be used to determine reflection coefficients, and thus surface properties, at a variety of locations on the Antarctic continent. The results of the HiCal experiment can be used in the reconstruction of the CR and neutrino events detected by ANITA. The design and engineering specifics for the first HiCal flight are discussed in Chapter 5. The analysis of the HiCal events in the ANITA data set and conclusions drawn from the analysis are presented in Chapters 6 and 7. The bulk of the work presented in Chapters 5 and 6 is the work of this author.

Chapter 2

Introduction to Cosmic Ray Extensive Air Showers

This chapter covers the general attributes of cosmic rays, how they produce extensive air showers in the earth's atmosphere, how those showers are detected by radio receivers, and how those measurements are used to reconstruct the pertinent properties of the primary cosmic ray.

2.1 Cosmic Rays

Cosmic ray (CR) is a broad term used to describe relativistic radiation of extraterrestrial origin that impacts the earth. Here, the term is reserved for the primary particle that produces a cascading particle shower following collision with a terrestrial or atmospheric nucleus. For clarity in this work, 'cosmic ray' will be used only for non-neutrino particles and when applicable, 'neutrino' will be used explicitly. High-energy gamma-rays are also considered to be CR but are outside of the definition used for this text.

The study of ultra-high energy cosmic rays and neutrinos is motivated by the efforts to determine the astrophysical processes that create them, accelerate them, and modify their trajectories through the universe. While the discovery and study of cosmic rays began in 1912 [1], interest and work in the field has waxed and waned over the last century, largely dependent on the achievable

energy range of man-made particle accelerators and developments in the detection techniques for ever higher energies of cosmic rays. Results from accelerator experiments are often used to extrapolate theories for higher energy particles and guide development of new cosmic ray detection experiments.

2.1.1 Production, Acceleration, and Propagation of CR

The lowest energy CR, <10 MeV, are produced in stellar nucleosynthesis and accelerated by stellar winds, flares, and coronal mass ejections [28]. For mid-energy CR, <3 PeV, supernovae are the most likely candidates for production and acceleration. The highest energy CR, up to the current detection limit of 500 EeV, have not been directly associated with sources or acceleration mechanisms but possible candidates are active galactic nuclei (AGN), hot spots, and intergalactic shocks. Figure 2.1, called a 'Hillas plot', shows these possible sources in terms of their magnetic field strength and physical extent. The red and blue lines on the plot are based on the Hillas criterion, [29], and give the cutoffs above which iron CR and proton CR may be accelerated to 10^{20} eV.

All CR are ions, either nuclei that have been stripped of electrons, or free electrons, meaning that their paths are affected by galactic and extra-galactic magnetic fields. These fields are not mapped or known to an extent that allows us to deconvolve their effect on the CR and thus it is not possible to point CR back to their source. However, inhomogeneity in arrival direction would indicate localized sources of production that can, in some cases, be correlated with other detections of gamma rays or neutrinos, for example.

CR arriving at Earth may be a true primary particle, or a secondary particle produced by the process of spallation as the primary interacts with interstellar matter, the Cosmic Microwave Background (CMB), or the Extra-galactic Background Light (EBL). Photopion and pair production occur from proton CR interacting with the CMB. Pair production and photo-disintegration occur when heavier nuclei interact with the CMB and EBL. These interactions occur with the highest energy CR and produce UHE neutrinos. Spallation of CNO and Fe cosmic rays increase the abundances of certain elements in the composition of the cosmic ray spectrum above what is measured

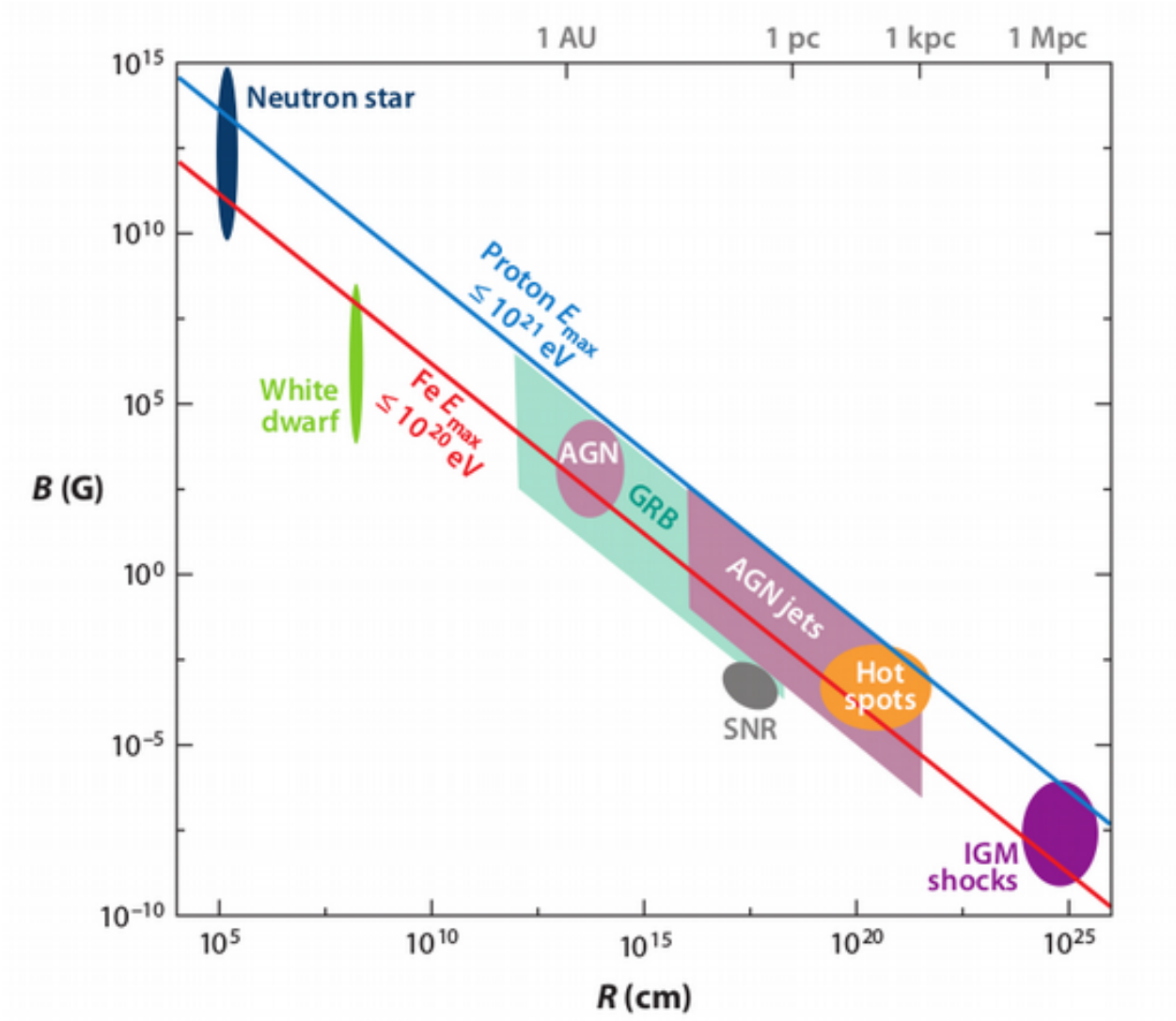

Figure 2.1: *Hillas plot showing possible sources of UHECR based on magnetic field strength, B, and radius, R, with minimum cutoffs shown for proton and iron CR of energy* 10^{20} *eV. Figure from [29]*

elsewhere terrestrially and in the solar system [30].

2.1.2 Understanding the CR Energy Spectrum

Figure 2.2 shows recent cumulative results of cosmic ray detections. The horizontal axis gives the measured or reconstructed energy of the primary particle and the vertical axis gives the flux or relative number of detected particles. There are three main features of importance in the cosmic ray energy spectrum: the knee, occurring at 3 PeV; the ankle, occurring at 4 EeV; and the high-energy cut-off at 500 EeV. Cosmic rays to the left of the knee are accelerated by supernova shock waves within our galaxy. The steepening of slope to the right of the knee indicates a decrease in the detected number of CR produced by this mechanism as energy increases. This may be due to: more of the higher energy CR having enough energy to escape the magnetic fields of the galaxy or from the shock fronts not being capable of accelerating the particles to higher energies, both of which should show a dependence on the primary mass.

The frontier in high energy astroparticle physics lies in increasing the statistics of CR detected above the ankle. In 1966, following the detection of the the CMB in 1965, it was theorized that an energy limit for detected CR existed at 50 EeV. The theory was based on assumptions that particles of energy above this limit would have to be created at distances far enough from earth that the probability of interacting with the photons of the CMB over that distance would fully attenuate the flux above that energy. However, as evident in Figure 2.2, particles above this cut-off energy have been detected by several experiments. There have been weak anisotropies measured at several points in the spectrum, including at the highest energies but increased statistics and separate measurements for CR of different masses are necessary to determine if these anisotropies point back to the actual sources of the CR [30].

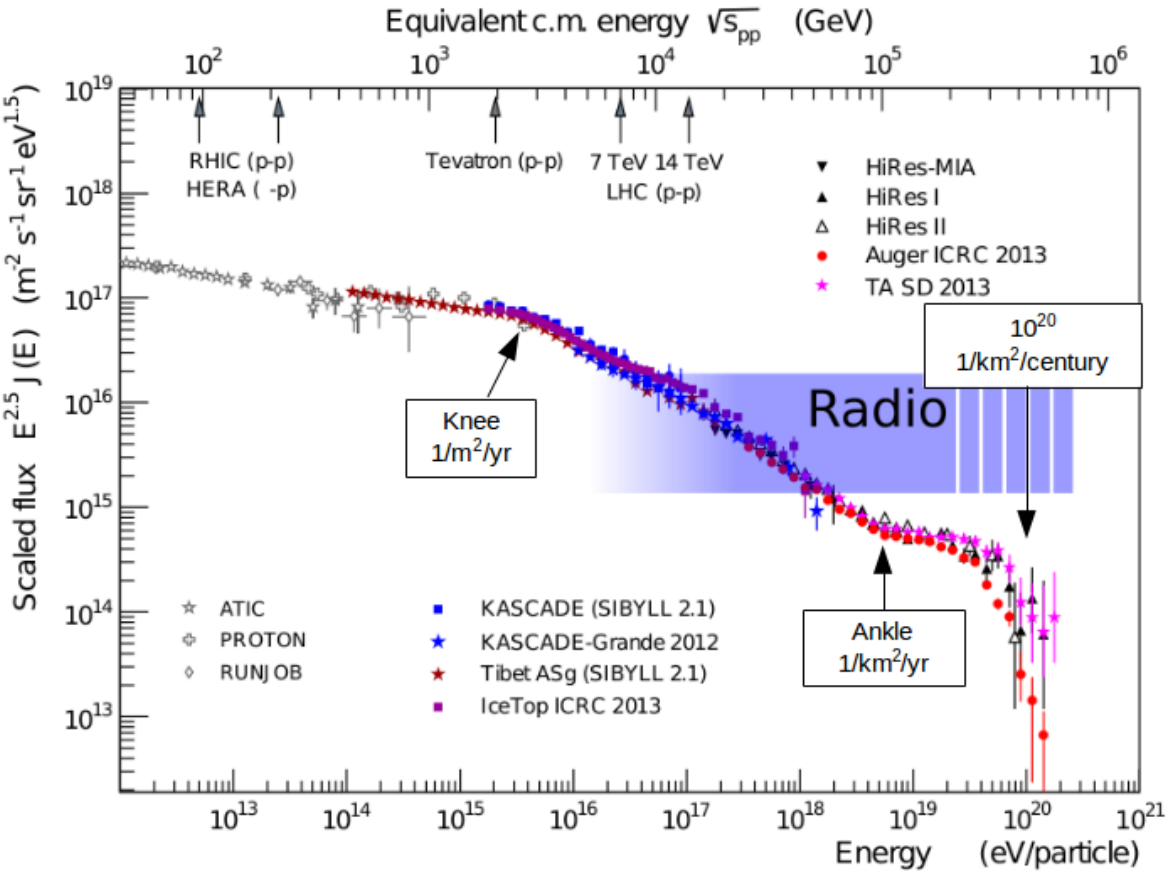

Figure 2.2: *Cosmic ray energy spectrum. Figure from [31] with labels added at the knee, ankle and* $10^{20}eV$*. The 'Radio' label denotes the energy range where radio detection is feasible.*

2.2 Cosmic Ray Extensive Air Showers

Cosmic ray extensive air showers (EAS) are particle cascades initiated when a primary particle (nucleon or nucleus) interacts with an atmospheric target. Fully developed EAS have three components: electromagnetic, hadronic, and muonic. The initial interaction largely produces charged and neutral pions but may, due to lower cross sections, produce charged and neutral kaons at much lower rates. The neutral pions will decay almost immediately into γ-rays which initiate the electromagnetic component of the air shower. Charged pions will either decay or re-interact depending on the particle energy and local atmospheric density. The likelihood of either event is expressed as 'radiation length' and 'interaction length', respectively. Radiation length is a material-specific characteristic that determines when a high energy particle will lose energy in a radiative process. Interaction length is based on the cross-section of possible interactions between the traveling particle and particles in the medium. For electrons in the atmosphere, radiation occurs via bremsstrahlung radiation and for photons it occurs by pair production. Due to time dilation, higher energy pions are more likely to re-interact than to decay and decays are more likely at higher elevations due to lower density. Charged pion decays produce muons and mu neutrinos, the muonic component of the shower. The hadronic component of the shower consists of the nuclear fragments from secondary interactions.

The overall number of particles produced in the shower as well as the relative number of particles making up the components depends on the initial energy and mass of the primary particle. Particle number increases exponentially until a maximum number of particles is reached (called shower-maximum) after which more particles are stopped or decay than are created. Since the processes of shower development are strongly dependent on the density profile of the medium, elevation values are generally given in terms of the atmospheric depth, X in g/cm^2, and X_{max} is the location of shower maximum. Showers develop both laterally and longitudinally. Lateral spread is governed by the transverse momentum of the bremsstrahlung, pair production, and Coulomb scattering interactions. The lateral extent of showers can reach up to several kilometers but the density of the particles is much higher toward the shower axis.

2.3 Coherent EM Radiation from Cosmic Ray Air Showers

An impulsive electric field created by time-varying currents that develop in the shower is due to two effects, the geomagnetic effect and the Askaryan effect. In air showers, the geomagnetic effect (transverse current) is the dominant contribution to the signal but is entirely negligible in dense media showers. The Askaryan effect is less pronounced in air showers than the geomagnetic effect but dominates the emission for showers in dense media like ice. The two effects are schematically described in Figure 2.3.

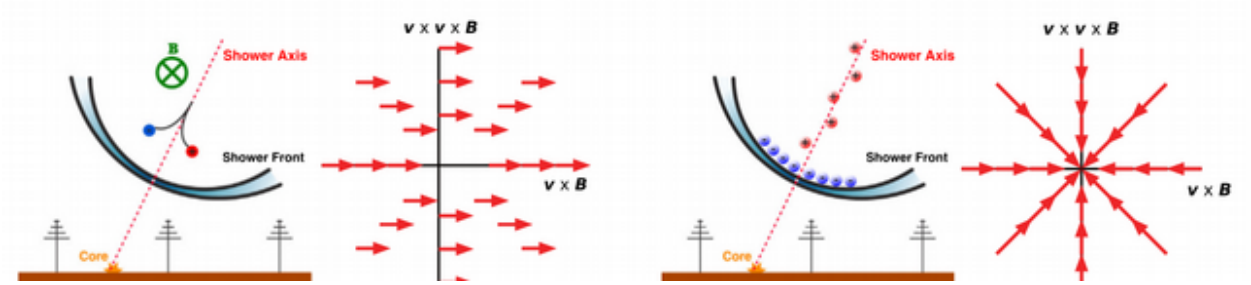

Figure 2.3: *Schematics showing charge positions and polarization on the ground relative to the earth magnetic field for the geomagnetic (left) and Askaryan (right) effects. Figure from [31]*

Following pair production, charge separation occurs due to the Lorentz force of the earth's magnetic field, producing the geomagnetic effect. It is still under some debate how to best model the emission caused by this effect. On one hand, it can be described as a dipole over the extent of the shower with time-varying charge. Alternatively, it can be described by having each individual particle emitting a signal due to the synchrotron effect of the paths in the magnetic field. The electromagnetic signal created can be described either microscopically as the sum of individual radiating particles, or macroscopically as the sum of the time-varying currents produced by these particles. In either case, the end result is a signal that is polarized in an East-West direction (along the Lorentz-force vector), the magnitude of which is dependent on shower inclination angle and local strength and direction of the magnetic field.

In the Askaryan effect, a significant negative charge excess (20-30%) [32] is produced by interaction of shower particles with atmospheric nuclei, specifically with the electrons of these nuclei. Positron annihilation reduces the positive shower component and ionization 'captures'

electrons into the shower, increasing the negative shower component. This results in a high density of negative charge close to the shower axis at the shower front. This is modeled as a radiating charge distribution, varying in time. The polarization of this emission is radially outward from the shower axis, as shown in Figure 2.3.

The signal from the two effects combines and is nearly coherent [30] for wavelengths above (frequencies below) the physical thickness of the shower front, which is generally about a meter, meaning frequencies below $\sim$300 MHz. This coherence means power scales quadratically with number of particles which scales with the primary particle energy. Due to the effects of relativistic particles moving in a non-vacuum, there is also a higher-frequency coherence, up to several GHz, confined in the direction described by the Cherenkov angle, θ_c given in Eq. 2.1, relative to the shower axis. This angle is $\sim 1^\circ$ in air. Figure 2.4 shows how the cone develops for a single particle.

$$\cos\theta_c = \frac{1}{n\beta} \tag{2.1}$$

Note that this does not mean the signal is Cherenkov radiation (visible light), but occurs at the Cherenkov angle because the particles and produced signal are traveling at nearly the same speed.

2.4 Reconstructing CR EAS Properties from Radio Detection

The goal from detecting EAS is to discern the primary particle mass, energy, and propagation direction. The shower axis defines the arrival direction and is determined based on arrival times of the signal at physically separated detector stations and is dependent in accuracy on the model used for the shower front shape [30]. Since heavier primaries interact higher in the atmosphere than lighter particles, measuring the location of shower maximum is a good indicator of primary mass. However, it is also necessary to measure the primary energy (shower energy) since it affects the atmospheric depth of the initial interaction as well.

Generally, the most accurate energy reconstruction is possible when the muonic and electro-

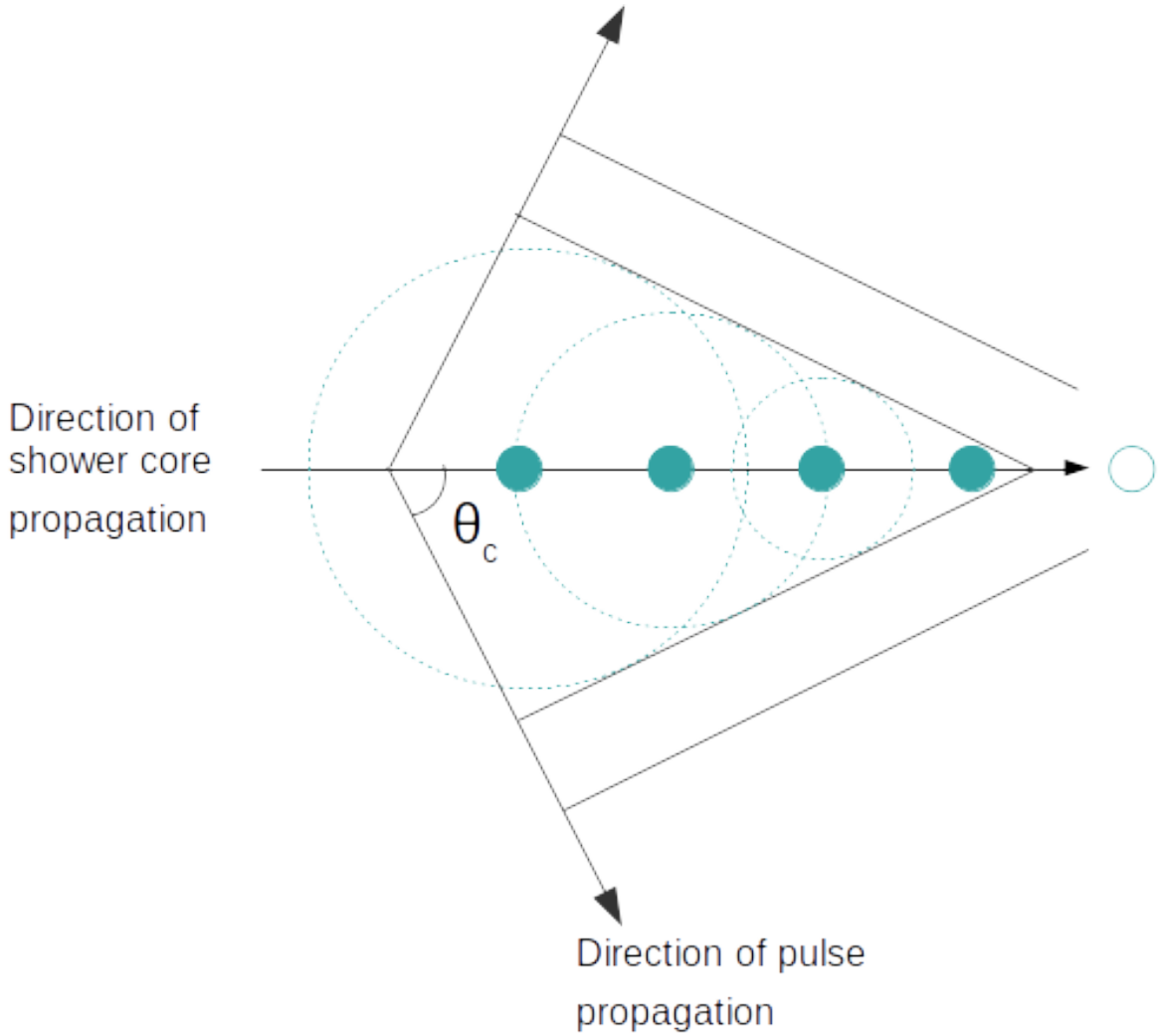

Figure 2.4: *Schematic showing the direction of travel and direction of EM radiation from a single particle moving relativistically. Since the particle and radiation are moving at comparable speeds, the produced pulse is coherent. The lifespan of the particle then determines the width of the cone.*

magnetic components of the shower are measured concurrently and at shower max, where the ratio between the two is the most accurately modeled. If however, the energy in the electromagnetic component is measured by the impulsive radio signal, measuring the muonic component is not strictly necessary because the peak in the radio signal occurs very near to shower max and there are other methods, using only the features in the radio signal, for determining the location of shower max. These methods are introduced in Chapter 6 of [30]. The method used by ANITA will be discussed in more detail in the next chapter of this work.

Chapter 3

Radio Detection of UHE Particles Showers in Antarctica

In the effort to detect high-energy astrophysical particles, Antarctica provides an appealing detection volume, especially for the experiments using radio techniques to detect neutrinos. The region is relatively devoid of anthropogenic noise and the ice sheets covering the continent provide a nearly homogeneous, dense, radio transparent media in which the particles can interact and shower, and through which the radio signals created can travel to a detector.

Study of the radio signal created by UHECR EAS began in the 1960s with measurements of showers occurring in the Earth's atmosphere. More recently, beginning in the late 1990s and continuing today, several radio detection experiments have been deployed in Antarctica (RICE [33], ANITA, ARA [34], ARIANNA [35]). ANITA, which will be discussed in more detail, is the only one of these experiments that is not ground based. While none of these experiments has yet detected a neutrino signal, ANITA and ARIANNA have detected CR EAS. The details of the ANITA detections are the subject of this chapter.

3.1 The ANITA Experiment

The ANtarctic Impulsive Transient Antenna (ANITA) experiment is a balloon-borne apparatus consisting of an array of dual-polarized radio frequency antennas carried at high-altitude, 38 km, and has a nearly 500,000 km^2 view of the ice-sheet. The ANITA-3 payload is shown in Figure 3.1. There have been five ANITA flights conducted so far (proof-of-concept ANITA-lite, 2003-04; ANITA-1, 2006-07; ANITA-2, 2008-09; ANITA-3, 2014-15; ANITA-4, 2016-2017). ANITA surveys the Antarctic ice surface looking for radio signals produced by ultra-high energy (UHE) neutrinos and cosmic rays. The payload is launched during the austral summer(s) when a circumpolar wind develops, allowing the payload to maintain a path above the continent. This path is critical both for collecting the data and for retrieving the data post-flight since the bulk of the data is only stored on-board (not transmitted during flight) and could not be recovered in the event of a water landing. The neutrino signals originating from shower events in the ice and the cosmic ray signals originating from shower events in the atmosphere arrive at ANITA after being, respectively, transmitted through or reflected from the air-ice interface. Currently, the ANITA cosmic ray data set consists of 18 total surface reflected events collected on the ANITA-1, 2, and 3 flights along with 2 events detected directly. The ANITA-4 cosmic ray analysis is still in progress.

Figure 3.1: *ANITA-3 being prepared for loading onto the launch vehicle at the Long Duration Balloon facility close to McMurdo Station, Antarctica.*

As discussed in the previous chapter, the geomagnetic and Askaryan effects produce different polarizations of the EM radiation. Since the magnitude of the polarization from each of these is different for in-air CR showers vs neutrino ice showers, from ANITA's viewpoint, neutrino signals will be predominately vertically polarized, while reflected cosmic ray signals will be horizontally polarized. This difference is due to the orientation of the Cherenkov cone relative to the signal path to ANITA, as shown in Figure 3.2. Due to differences in the triggering schemes between ANITA-1 (h-pol and v-pol) and ANITA-2 (emphasis on v-pol), the majority of the reflected CR events (14) were detected by ANITA-1. It is possible to determine the difference between direct and reflected CR events both by the arrival direction (above or below the horizon) and by the phase of the signal since the reflected h-pol signals undergo a phase inversion. Several improvements were made to the ANITA-3 trigger that should increase the acceptance of EAS events. Previously, for an event to trigger, power thresholds in multiple sub-bands of the frequency spectrum had to be met but ANITA-3 and ANITA-4 use the full frequency band. Since events viewed away from the Cherenkov cone angle have falling spectral slopes, the previous ANITA flights had a stronger geometric limit on the number of triggered EAS events. Additionally, a low frequency (75 MHz) bicone antenna was included in the ANITA-3 flight, extending the triggerable frequency range.

Over the ANITA frequency range, 200-1200 MHz, the coherent radio pulse propagates along the Cherenkov cone, as discussed in the previous chapter. Figure 3.3 gives an example of how this signal intersects the ground in a ring pattern, the shape and size of which is determined by the inclination angle of the shower and altitude of the first interaction.

3.2 Interferometry

As mentioned above, the ANITA experiment consists of an array of dual-polarized antennas sensitive to the frequency range 200-1200 MHz. Impulsive events are identified in the data set using interferometric methods. The antennas are mounted with bore-sights pointing 10° below horizontal and have a 45° beamwidth creating a field of view covering all azimuthal angles and +35/-55°

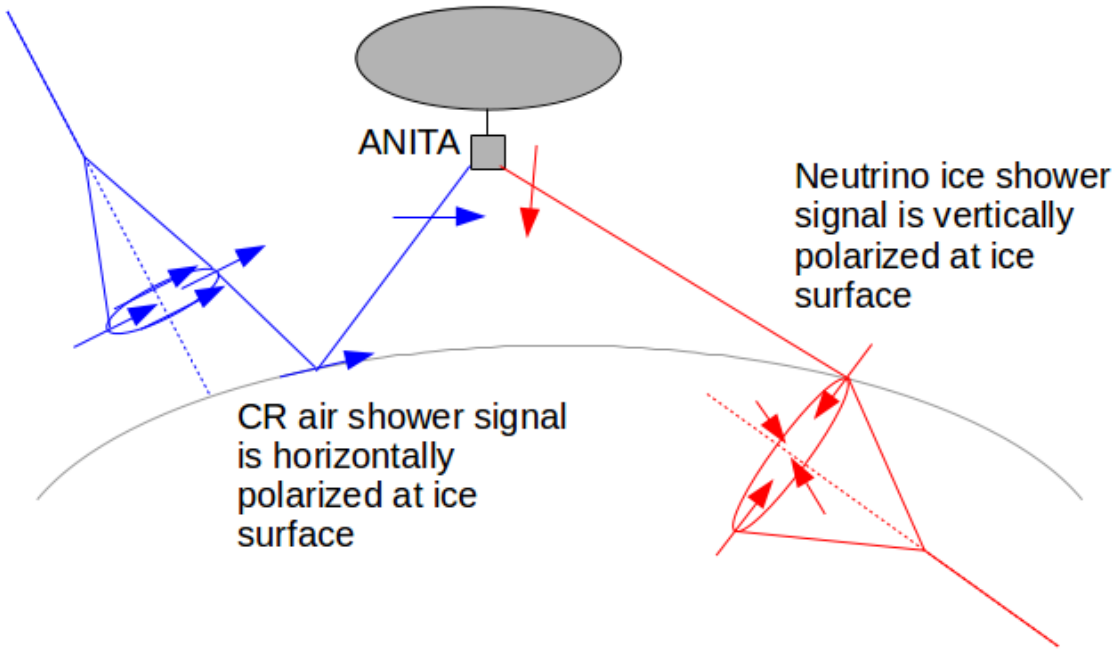

Figure 3.2: *Comparison between the polarizations of the radio signal arriving at ANTIA from a reflected in-air shower (left,blue) and an in-ice shower (right, red). The domination of the Askaryan effect in the ice causes the transmitted signal to be vertically polarized, while the geometry of the in-air signals produces a predominately horizontally polarized signal.*

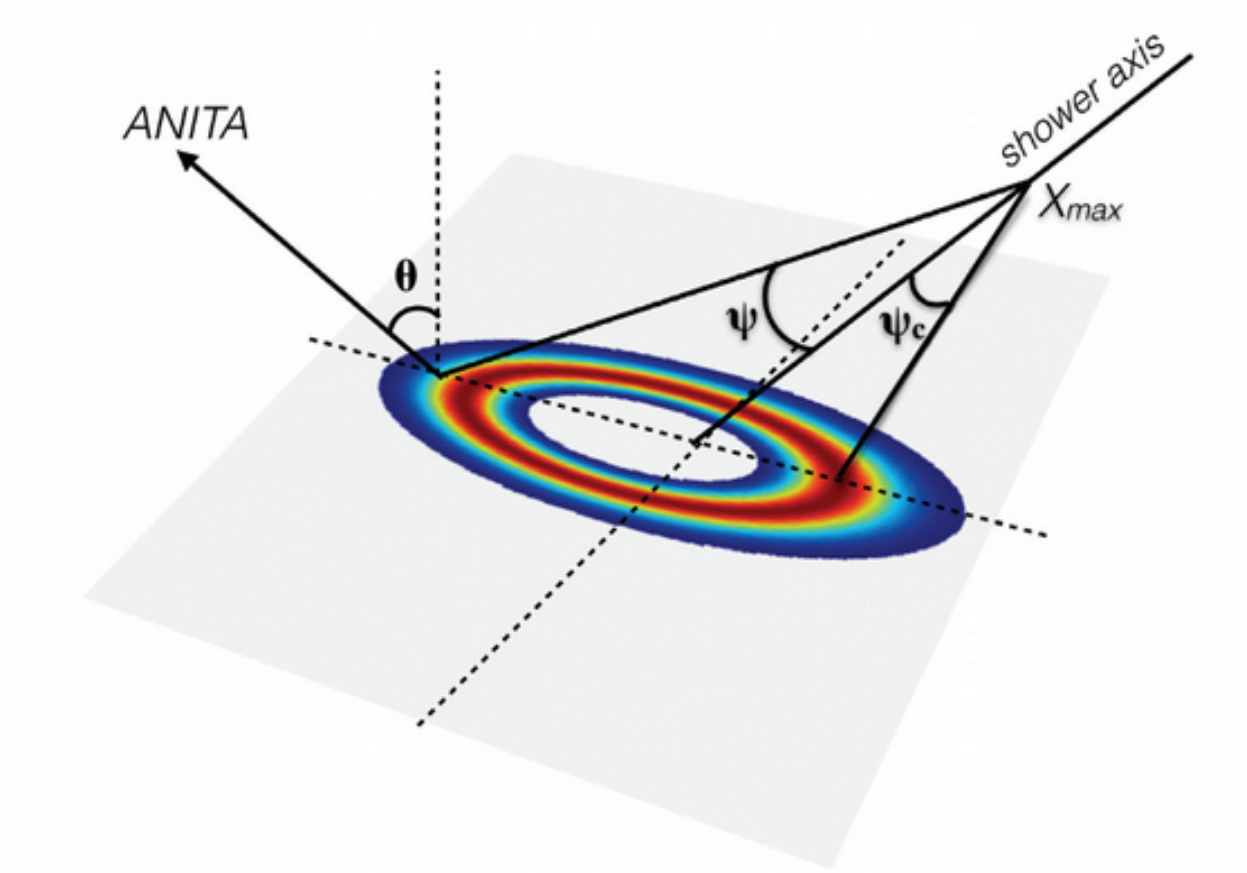

Figure 3.3: *Example of the footprint of a CR EAS event on the ground, showing the shower axis, Cherenkov anlge* Ψ_c *and detected angle* Ψ*. Figure from [37].*

relative to horizontal in altitude. The ANITA antennas are assigned to phi-sectors based on each antenna bore-sight direction. There are 16 phi-sectors, each sector including two or three antennas depending on the generation of the experiment. The post-flight analysis of the recorded events involves first determining which events are potentially interesting from the physics perspective. For a given event, signals from antennas with overlapping beam patterns are cross-correlated (CC) pairwise creating a correlation-vs-delay plot. A recorded event example is shown in Figure 3.4. Each highlighted antenna on the left corresponds to one of the waveforms on the right. Figure 3.5 shows three examples of pairs from this event with their correlation-vs-delay plots and the values from this plot mapped back onto the sky view. Each CC value represents the level of coherence of a signal originating on a plane that is perpendicular to the baseline of the antenna pair and defined by the value of the delay and distance between antennas. The CC values are produced for all pairs of antennas, creating a coherence map over the entire field of view of the experiment, the result of this is shown in Figure 3.6. For each event's coherence map, a peak search is conducted. Single, strong peaks are identified as impulsive events of interest. Cuts are made to this list of interesting events based on pointing location (events close to base and traverse locations are removed, for example), and the remaining events are further analyzed.

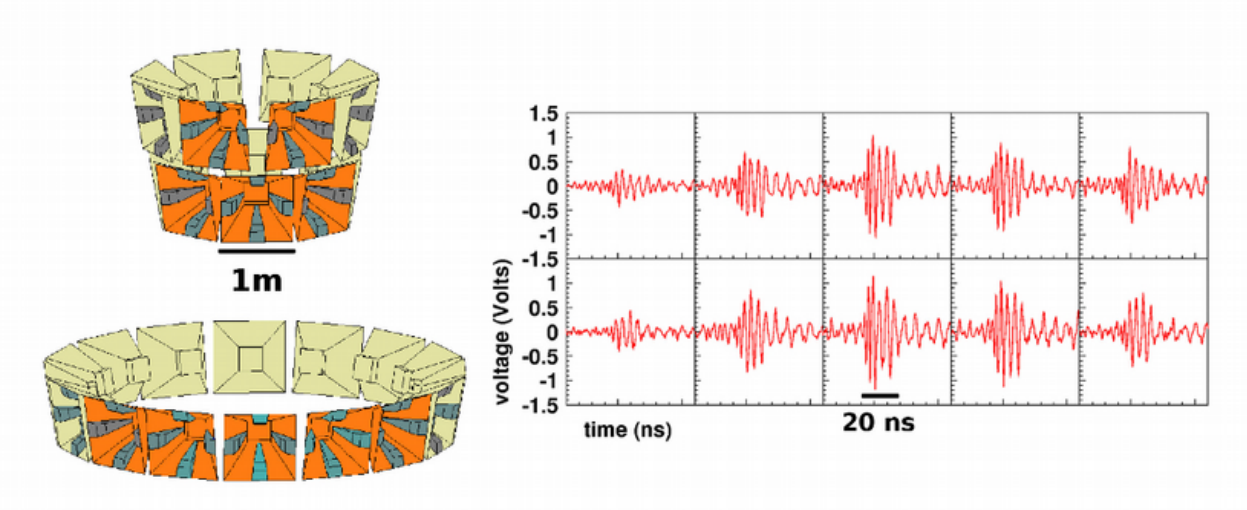

Figure 3.4: *Diagram on the left shows 10 antennas corresponding the 10 waveforms on the right for a single event recorded during flight. Figure from [36].*

For an event identified through the interferometry method and passed through the cuts, signals

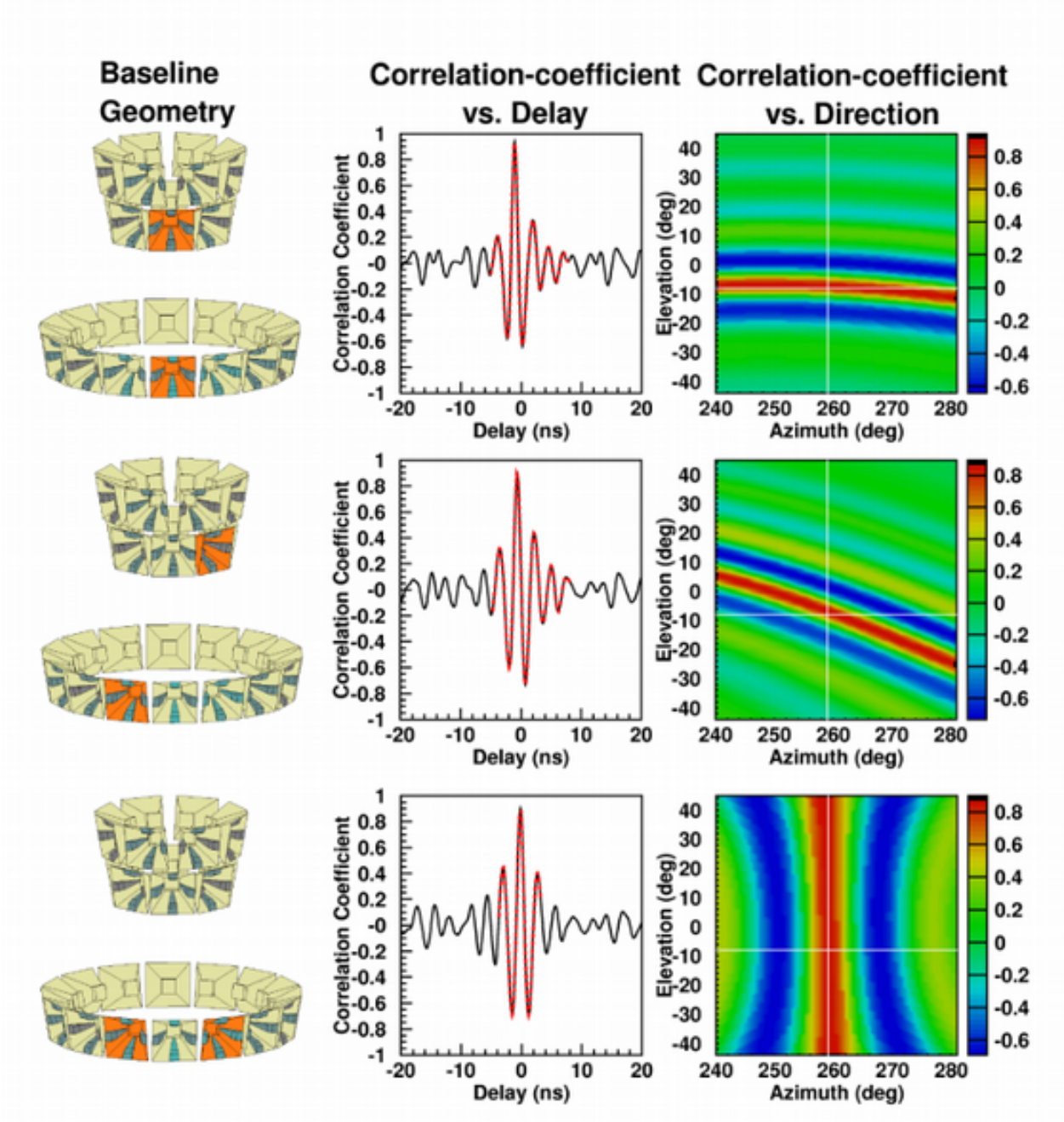

Figure 3.5: *Three examples of pairwise cross-correlation are shown with the antenna pairs highlighted (left), the correlation-coefficient plot (middle) and the correlation-coefficient values mapped onto the field of view of the antenna pair (right). Figure from [36].*

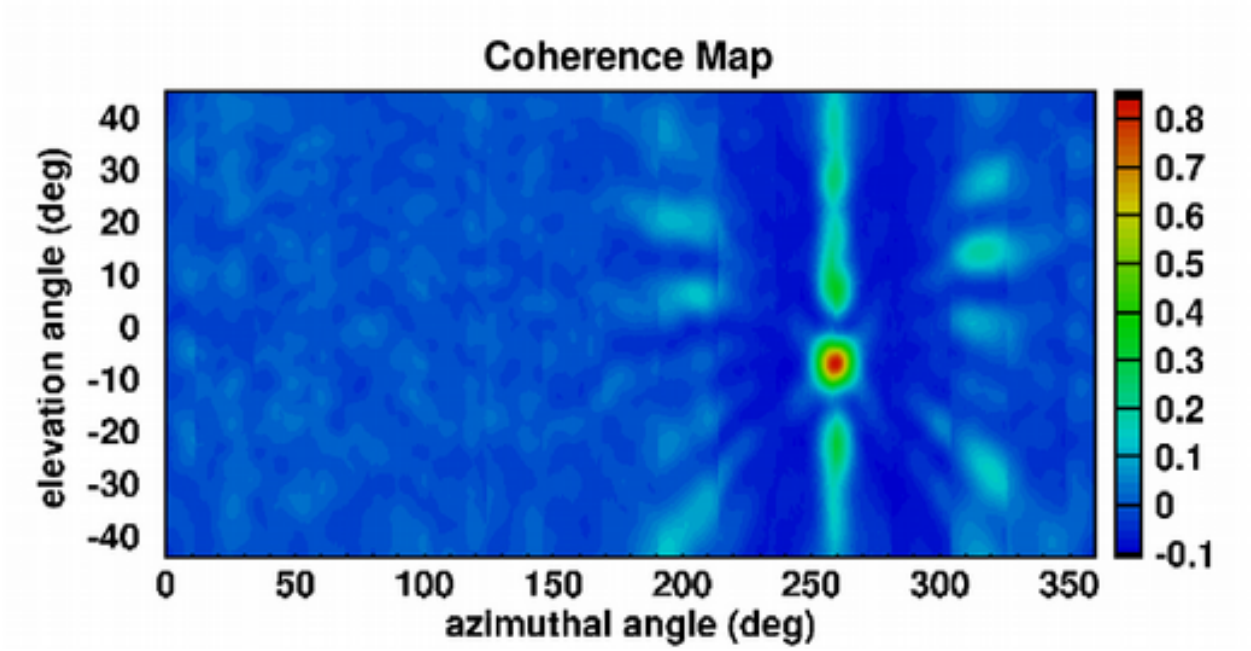

Figure 3.6: *Full sky-map produced by summing and averaging all pairwise correlation-coefficient maps. Figure from [36].*

from the antennas pointing to that event are selected, phase aligned and summed to create a coherently summed waveform (CSW), Figure 3.7. This coherently summed waveform is used for extracting the information necessary to do event reconstruction.

3.3 Event Reconstruction

Reconstruction of each cosmic ray event involves determining the pointing direction and energy of the primary particle. Energy reconstruction uses the the slope of the event frequency spectrum which depends on both the event energy and the viewing angle relative to the Cherenkov cone angle. See Figure 3.3. Monte Carlo simulations are implemented to produce frequency spectra which are then used to determine an appropriate fit function for the event spectra. Figure 3.8 shows the waveforms for a detected and simulated CR event and the frequency dependent waveform amplitudes. Based on the simulations, the fit function is a simple exponential of the form

$$A_f(f) = Ae^{\gamma(f-300\text{MHz})} \tag{3.1}$$

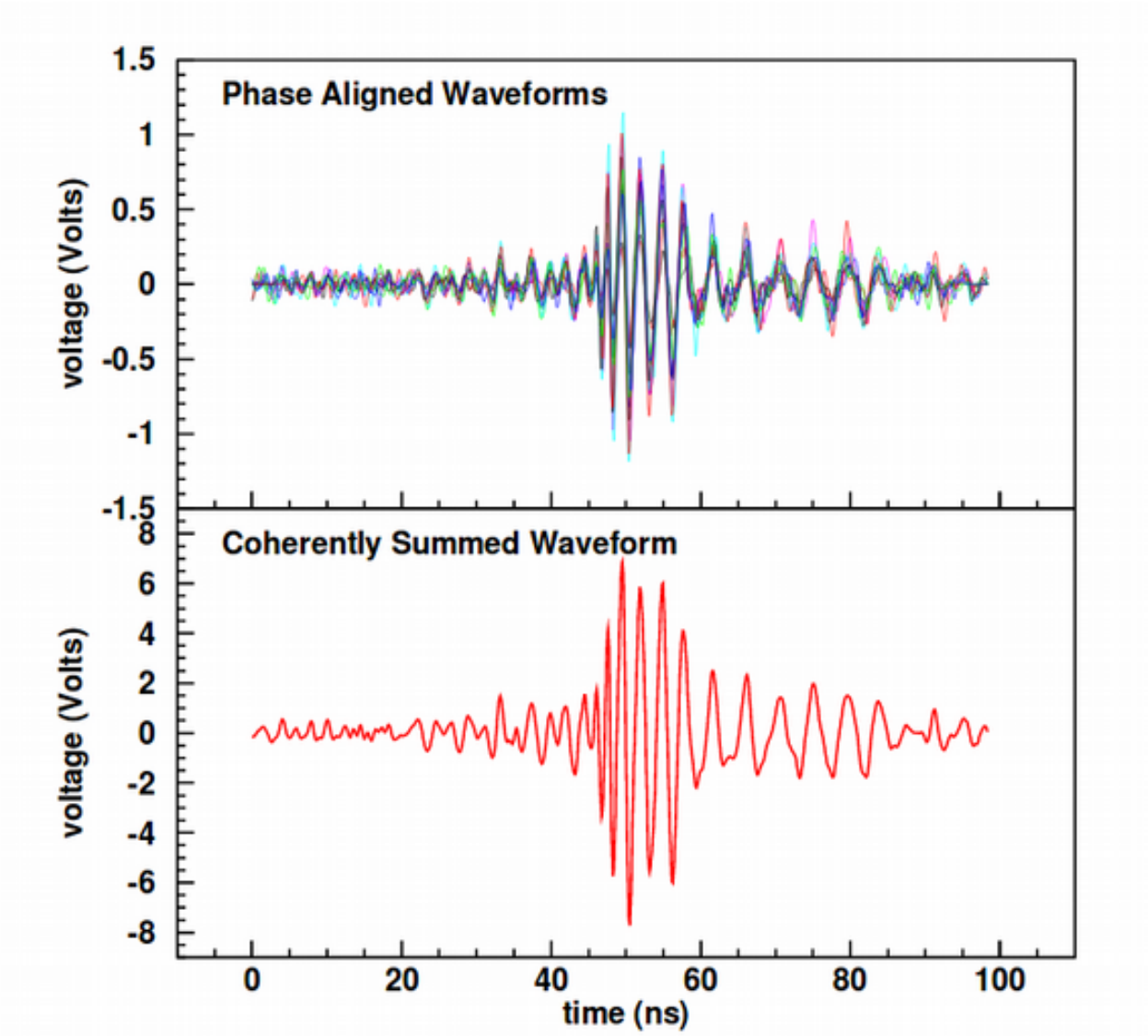

Figure 3.7: *Example event showing the phase aligned waveforms from multiple antennas (top) and the coherently summed waveform (bottom). Figure from [36]*

Both A and γ are a function of the off-cone angle ψ, with maximum values for $\psi = \psi_C$. Furthermore, there is a simple linear relationship between $log_{10}A$ and γ:

$$\log_{10}(A) = \log_{10}(A_c) + b(\gamma - \gamma_c) \tag{3.2}$$

The simulations show that A_c is directly proportional to the primary energy. Once A and γ are determined from the data, b and γ_c are determined by simulating showers in the range of energies of interest. From here, Equation 3.2 is used to find the value of A_c for a given observed shower.

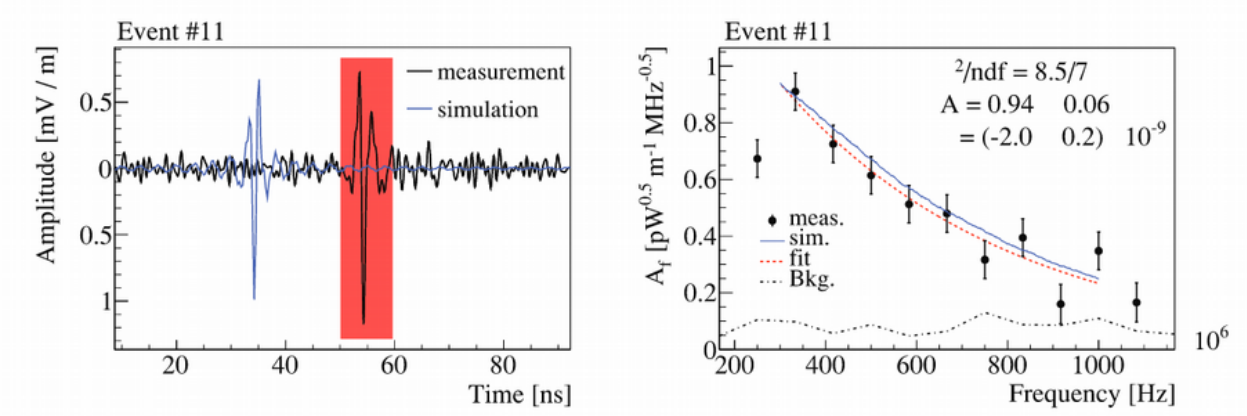

Figure 3.8: *An example of a recorded (black) and simulated (blue) CR event detected by ANITA are shown on the left. The frequency dependent amplitudes are given on the right with the fit to Equation 3.1. Figure from [37].*

Of the 20 cosmic ray events detected by ANITA thus far, 18 were detected as reflections from the ice surface. Reconstruction of these EAS events, and any future neutrino events, requires characterization of both the detection instrument as well as the natural environment, the atmosphere and the ice, in which the interactions take place. While significant effort has been made to study the Antarctic surface properties, largely for the purpose of climate studies, there is limited previous work in the frequency band of interest in radio cosmic ray experiments. As a result, one of the uncertainties in energy reconstruction of the shower events arises from the unknown effect of surface roughness.

Chapter 4

Surface Roughness in Antarctica

The study of the roughness of natural surfaces has largely been in the domain of metrology as it applies to geology and climatology since it plays an important role in energy transfer and material transport. Specifically in Antarctica, surface roughness is necessary to measure and model in order to understand accumulation and melting rates and wind transport of the surface layers of snow.

Accumulation, moisture content, wind speed and direction, and snow grain size can all affect the size and shape of structures on a snowy surface. Geographic variation of these parameters can produce vastly different surface features at different locations in Antarctica. In some locations, ground measurements of windblown features known as sastrugi report surface height (0.10 to 0.25 m) and width (0.7 to 4.0 m) [38] values that are similar in scale to the wavelength regime used by ANITA. These surface features could produce loss of coherence or shadowing that would result in a decrease in the received power from the reflection. In the context of cosmic ray and neutrino EM shower detection, it would be ideal to quantify this effect of surface roughness in the frequency range of 100-1200 MHz. This frequency range is not of particular interest for study outside of the field of high energy physics and is more difficult to study than higher frequencies due to increasing size of the required antennas. Consequently prior to the work done with or for the ANITA experiment (covered in the Passive Receivers section below and in Chapters 5 and 6), all measurements have been performed outside of this range.

4.1 Modeling Roughness for Application to ANITA Analysis

Three approaches to modeling surface roughness for application to the ANITA analysis will be discussed here, one using a ray-tracing method and two employing numerical integration techniques [39, 40]. The two numerical integration methods were performed in the ANITA frequency band and over the scales typical of a CR EAS reflection. The ray-tracing method, developed by this author, was conducted in the frequency range of 2-3 GHz in order to complete a direct comparison with reflection data taken in the lab.

One of the numerical integration methods starts from reflection of a smooth flat surface using correction factors to address earth curvature and roughness [39]. The other starts from a general description of reflections from a smooth spherical surface [40]. Both of the integration approaches use scalar Kirchoff (Rayleigh-Sommerfeld) theory for smooth surfaces adding roughness with a fractal self-affine approach and the Rayleigh roughness criterion. The fractal self-affine approach is largely laid out in [41] and [42] and uses a combination of RMS height and Allan deviation to characterize the scale of the surface roughness. Here, the RMS height (4.1) and Allan deviation (4.2) are given for a 2D profile (height, z, and distance, x, along a single direction on the surface) but when applicable can be transformed to the 3D case where measurements would be taken along two axes. The 2D case is used here since that is the method that ANITA used.

$$\sigma_h(x) = \sqrt{\frac{\sum_{i=1}^{n} (z_i(x) - \bar{z})^2}{n-1}} \tag{4.1}$$

where $\bar{z}$ is the average height over the entire profile

$$\alpha(\Delta x) = \sqrt{\langle (z(x) - z(x+\Delta x))^2 \rangle} \tag{4.2}$$

The Hurst parameter, H, is found by fitting the measured data using either the Allan deviation or RMS height since they have similar relationships given in Equations 4.3 and 4.4.

$$\alpha(\Delta x) = \alpha(\Delta x_0)\left(\frac{\Delta x}{\Delta x_0}\right)^H \tag{4.3}$$

$$\sigma_h(L) = \sigma_h(L_0)\left(\frac{L}{L_0}\right)^H \tag{4.4}$$

For ANITA, hand measurements of surface height were taken over a single 120 meter track from one location near Taylor Dome. In areas of Antarctica where sastrugi are present, using the 2D method would probably not suffice as the sastrugi are generally aligned in a striation pattern, meaning a 2D profile along the sastrugi ridges may produce a very different Hurst parameter then a 2D profile going across the ridges. The ice surface around Taylor Dome, however, is fairly devoid of sastrugi. Consequently, the 2D profile data collected was used to calculate the Allan deviation (4.2), and determine the Hurst parameter for this data which is used to quantify how the roughness scales over the range of the first Fresnel zone, corresponding to a length scale of up to $\sim$300 m for the near nadir regime. The effect of this roughness is converted to a roughness factor using (4.5) which is then applied as a scaling factor to the magnitude of the reflected electromagnetic field. This approach is considered to be valid as long as σ_h over the reflection area is less than the smallest wavelength used to measure the reflection.

$$\frac{E_{rough}}{E_{smooth}} = F(k,p,\theta) = exp(-2k^2\sigma_h(\rho)^2\cos^2(\theta_0)) \tag{4.5}$$

Fresnel zones are used to denote ranges between a transmitter and receiver where rays reflected at that range will coherently or decoherently interfere with a specularly reflected ray. The cutoff for each zone is determined by the phase difference, $\Delta\phi$, between the direct and reflected path. The boundary for the first Fresnel zone is $\Delta\phi < \pi/2$. Equation 4.6 gives the Fresnel zone radius, $r_{Fn,LOS}$ for line of sight relation for each zone, n.

$$r_{Fn,LOS} = \sqrt{\frac{n\lambda d_1 d_2}{d_1 + d_2}} \tag{4.6}$$

For reflections, an approximation of the Fresnel zone radius is used given by $r_{Fn,refl} = r_{Fn,LOS}/\cos\theta$. In the case of ANITA, for the typical altitudes of the payload and initial shower interaction, the footprint of the impulsive signal on the ground is within the first Fresnel zone.

For the horizontal polarization and σ_h=0.15 m, Figure 4.1 shows (4.5 at the bounds of the ANITA frequency range, 200-1200 MHz, and this roughness model applied to the Fresnel predicted amplitude reflection ratios. The results of the numerical models are shown in Figure 6.15 in comparison to the HiCal and solar reflectivity data.

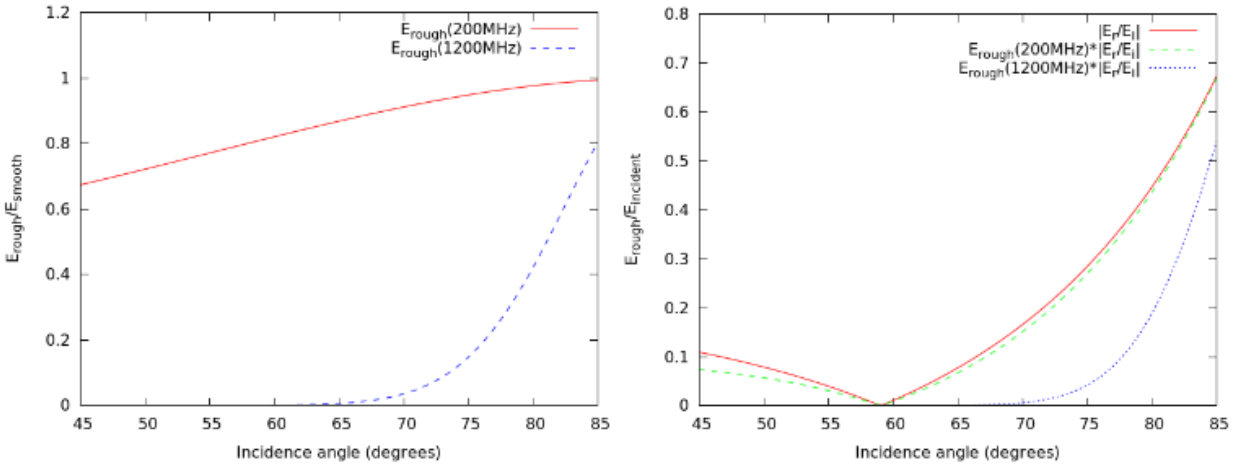

Figure 4.1: *Left panel shows the ratio of rough:smooth reflected amplitudes at 200MHz (solid red) and 1200MHz (dashed blue). Right panel shows this ratio applied as a correction factor to Fresnel predicted amplitude reflection ratios along with the Fresnel curve for a smooth surface (solid black).*

For reflection measurement systems using a transmitting (Tx) and receiving (Rx) antenna, the received to transmitted power ratio can be described by (4.7)

$$\frac{P_r}{P_t} = \frac{G_t G_r A \lambda^2}{(4\pi)^3 (d_1 d_2)^2} F_{fresnel}(\theta) F_{rough}(\theta, h, f) \tag{4.7}$$

where P_r and P_t are the transmitted and received power, G_t and G_r are the transmitter and receiver gain, A is the area of a surface element and d_1 and d_2 are the the Tx $\rightarrow$ surface and surface $\rightarrow$ Rx distances. The gains are measured in free space as a function of elevation and azimuth angle relative to the the antenna boresight. The power ratio is measured from the CW or impulsive signals, A is user defined, and the distances are calculated from the antenna position. For dielectric

materials, $F_{fresnel}$ varies with incidence angle as shown in Eq. (4.8) and Eq. (4.9) for horizontal and vertical polarizations respectively. It is then left to determine the form of $F_{rough}(\theta, h, f)$.

$$r_h = \frac{n_1 cos\theta_i - n_2 cos\theta_t}{n_1 cos\theta_i + n_2 cos\theta_t} \tag{4.8}$$

$$r_v = \frac{n_2 cos\theta_i - n_1 cos\theta_t}{n_1 cos\theta_i + n_2 cos\theta_t} \tag{4.9}$$

For the ray-tracing facet approach, the surface is divided into gridded sections and the signal is treated as a collection of rays emanating from the Tx antenna to each facet on the surface. Following reflection from a facet or directly by line of sight, rays that are directed toward the Rx antenna are used to calculate the received power. The pair of antennas are moved through a range of vertical positions to achieve a range of viewing angles (incidence or elevation angles) toward the center of the grid. At each set of antenna positions, antenna gains and Fresnel coefficients are applied according to the angular directions between the antennas and the surface elements. For a single flat foil facet the amplitude seen by the receiver is given in (4.10)

$$A_r = \frac{A_t F_{fresnel} \sqrt{G_t(\theta_t, \phi_t) G_r(\theta_r, \phi_r)} e^{i\phi}}{(4\pi)^{3/2} d_1 d_2} \tag{4.10}$$

The transmitted amplitude A_t is taken to be 1 for each ray and the sum of all amplitudes is normalized by the number of rays used. So far, this model has been compared to the flat foil surface measurements. Initially, a single direct and single reflected ray were used, but this was inadequate to describe the measurements, as shown in Figures 4.2 and 4.3. The number of rays was increased, effectively increasing the size of specular reflection on the surface, and varied according to the elevation angles of the antennas. The results of this adjustment are shown in the same figures. While the results are a closer approximation than the 2-ray method, there are still significant deviations especially at the higher frequencies. It has been noted [43] that the ray-tracing facet method has limitations especially in the radio frequency range and may require additional approximations to be applied to the reflection coefficients. It was attempted to extend this method for comparison

against roughened, dielectric surfaces with inadequate results.

4.2 Measuring Surface Roughness

A variety of techniques can be used to measure the surface features of a natural terrain: photogrammetry, radar imaging, lidar mapping, and contact profilometry. The following subsections provide details for previous measurements of the Antarctic ice sheet surface using a variety of different active and passive radar systems.

4.2.1 Monostatic Radars

Monostatic radars are those where the transmitters and receivers are co-located. This setup is common for use in remote sensing satellite radar systems. These systems are somewhat limited in the reflection data that they can obtain because they can only operate in the near-nadir regime or over a range of incidence angles, but restricted to backscatter measurements anti-parallel to the forward beamed signal. These systems, [44][45], have been extensively used to map reflectivities over Antarctica in the 1-40 GHz frequency ranges. Figure 4.4 shows data from four of these satellite based radars. Comparing location specific reflectivity values, the three higher frequency bands show high correlation values with each other and are anti-correlated with location specific wind velocities, as might be expected.

4.2.2 Passive Receivers

In a first attempt to quantify the location dependent Antarctic ice surface roughness in the 200-1200 MHz regime, we used data from the ANITA-2 flight [47](2008-09) and ANITA-3 flight [46] to measure the solar signal and determine the direct:reflected power ratio . To do this, the time-series voltage waveforms received by the ANITA antennas, separately for the horizontal and vertical polarizations, are cross-correlated to produce event-by-event correlation maps, as described in Section 3.2. A direct- and reflected- solar image tracking script is implemented to produce multi-

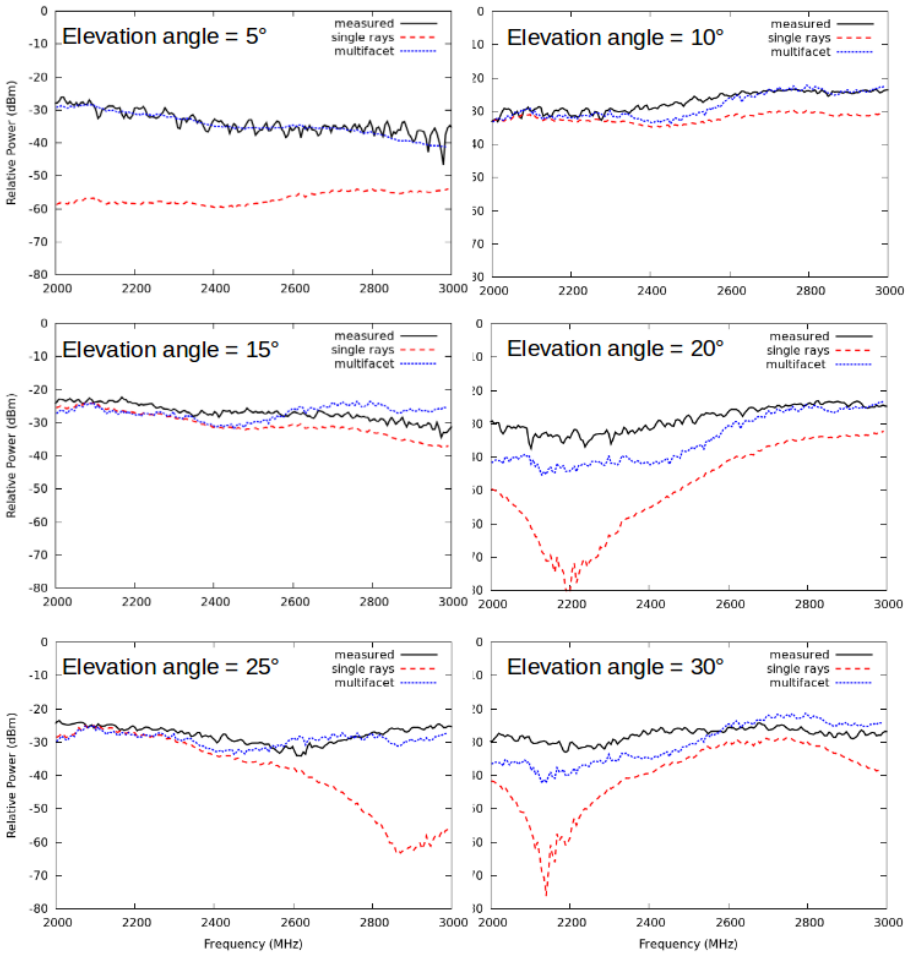

Figure 4.2: *Comparison of ray-tracing model to VPol measurements on flat foil over a range of elevation angles. Black traces are measured spectra, red dashed lines are the two-ray method, and the blue lines are from the multi-ray method.*

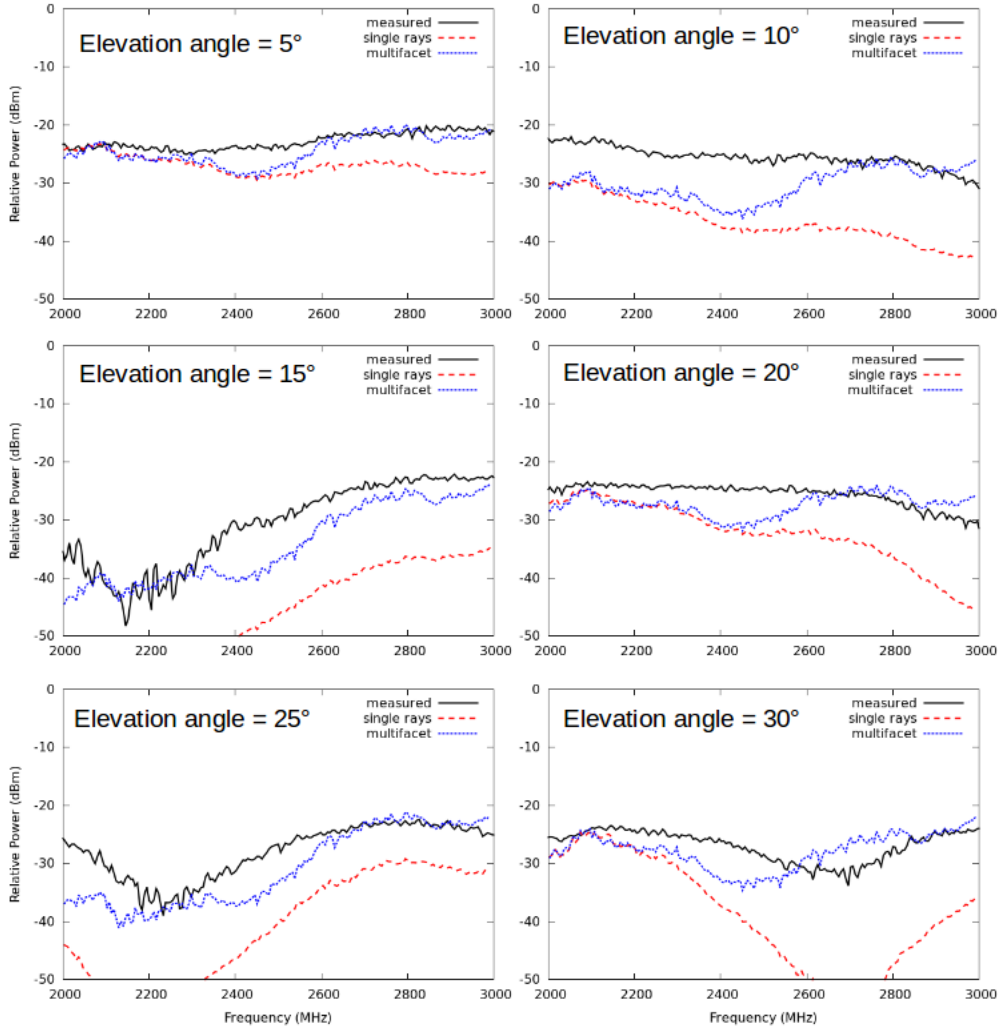

Figure 4.3: *Comparison of ray-tracing model to HPol measurements on flat foil over a range of elevation angles. Black traces are measured spectra, red dashed lines are the two-ray method, and the blue lines are from the multi-ray method.*

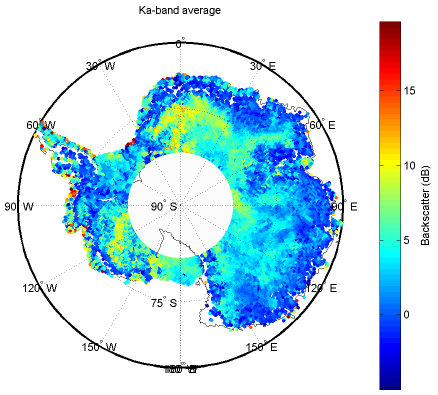

(a) Ka-band (26.5–40 GHz) Antarctic surface reflectivity, drawn from Envisat satellite data.

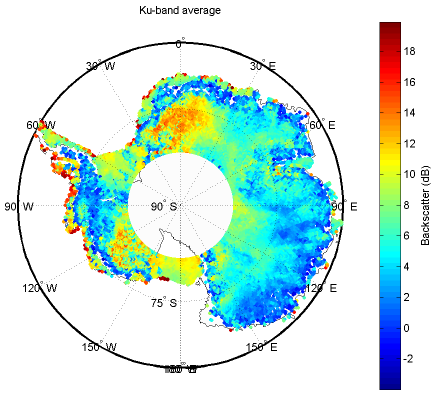

(b) Ku-band (12–18 GHz) Antarctic surface reflectivity, drawn from Envisat satellite data.

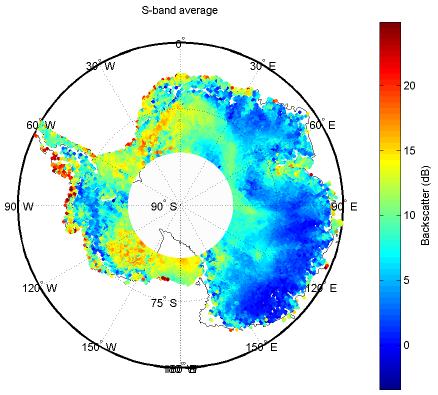

(c) S-band (2–4 GHz) Antarctic surface reflectivity, drawn from Envisat satellite data.

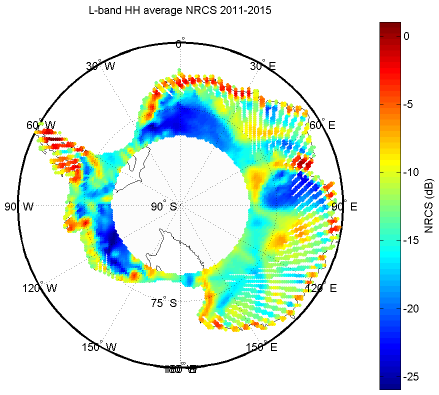

(d) L-band (1–2 GHz) Antarctic surface reflectivity, (HPol transmitter and HPol receiver) drawn from Aquarius satellite data.

Figure 4.4: Compilation of satellite reflectivity data. Figure from [46]

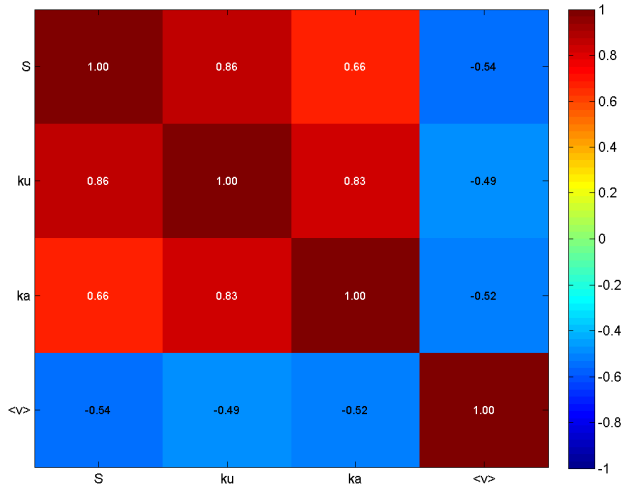

Figure 4.5: *Correlation between S-band, Ku-band, Ka-band reflectivities, as well as correlation with wind velocities. Figure from [46]*

event correlation maps in order to increase the solar and reflected signal SNR and extract power measurements. These measurements showed little variation from the predicted Fresnel reflection coefficients as shown in Figure 4.8, except at low elevation angles. There are several reasons these measurements are not ideal for determining the effect of surface roughness for the radio EAS signal. The solar signal is a non-impulsive, CW source with low single event SNR, requiring that the power be extracted from the summed interferograms instead of using single event coherently summed waveforms as is done for EAS events. While we attempted to do a frequency dependent reflectivity analysis, the solar frequency spectrum, shown in Figure 4.7, and the frequency response of the antennas produce a signal spectrum that falls with frequency to the extent that the solar signal can only be extracted for the lowest frequency band. Consequently, this analysis did not provide any frequency dependent information about the surface roughness. And finally, the range of solar inclination angles (12-35°) does not provide data for the most oblique incidence angles, where nearly half of the ANITA UHECR events occurred and where reductions in reflected signal amplitude will be greatest.

The same data from Figure 4.8 are shown in Figure 4.9 as a function of elevation angle. The points are the averages of the data binned in 1° increments and the errors are the RMS values for

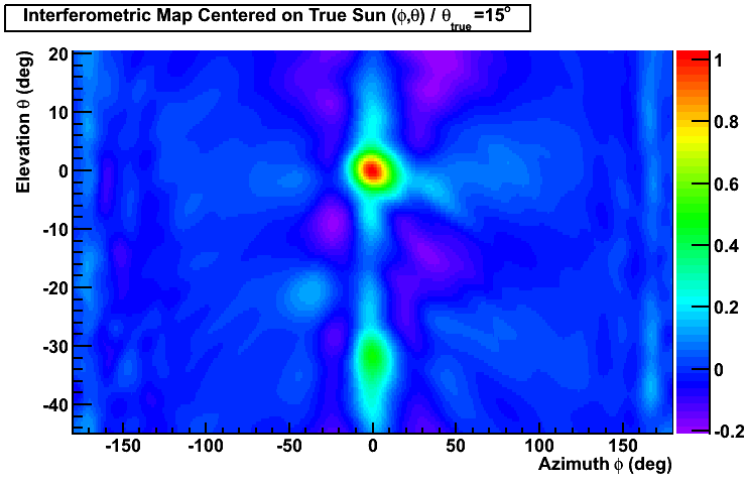

Figure 4.6: *Sample ANITA-3 sun-centered interferogram showing solar radio frequency image (at* $(\phi, \theta \sim 0,0)$*) and reflection (at* $(\phi, \theta) \sim (0, -20)$*).*

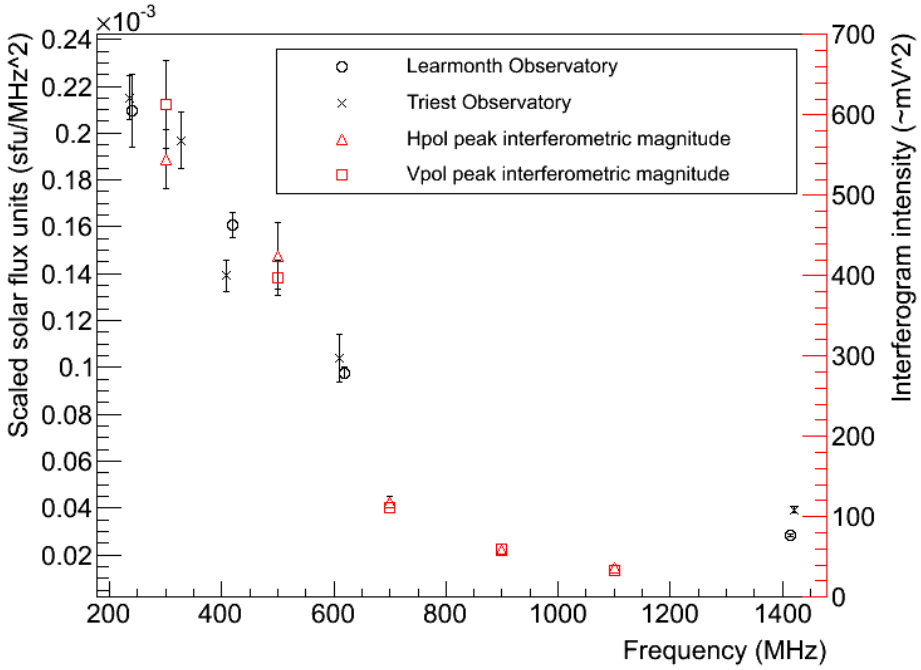

Figure 4.7: *Comparison of direct solar power as received by ANITA-2 and from several solar observatories.*

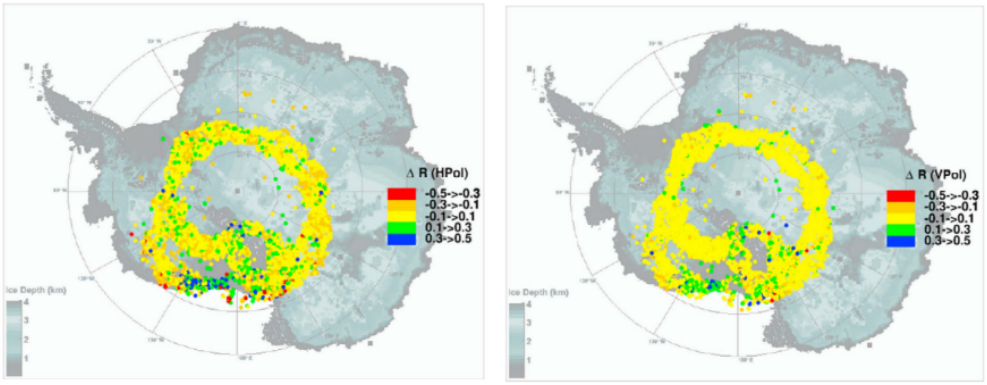

Figure 4.8: *Deviations from Fresnel predicted reflection coefficients in the horizontal (left) and vertical (right) polarizations.Legend at the lower left of each frame gives the ice thickness. Legend at the right of each frame shows the difference between the measured solar reflection coefficients and the predicted Fresnel coefficients assuming a refractive index typical of ice of 1.35.*

each bin.

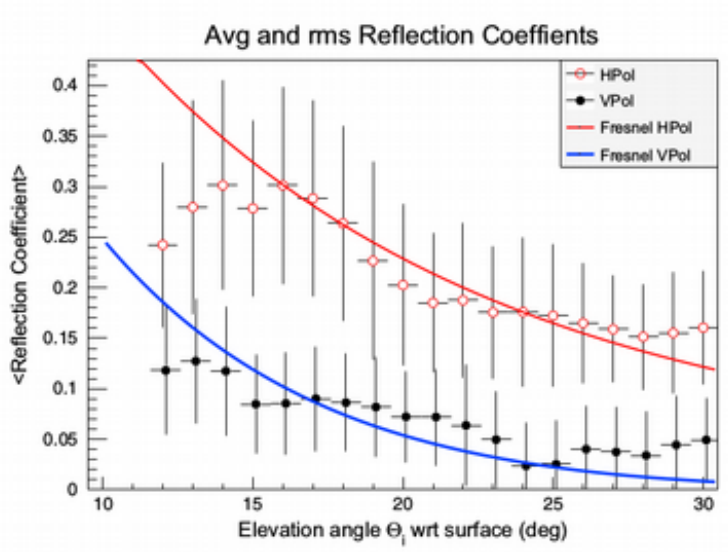

Figure 4.9: *HPol and VPol reflection ratios are shown as the data points and the predicted Fresnel curves are shown as solid lines.*

The variation of measured coefficients with respect to the predicted Fresnel coefficients implies an additional uncertainty from surface roughness adjustments applied to CR energy reconstruction, shown in Figure 4.10 as a function of elevation angle.

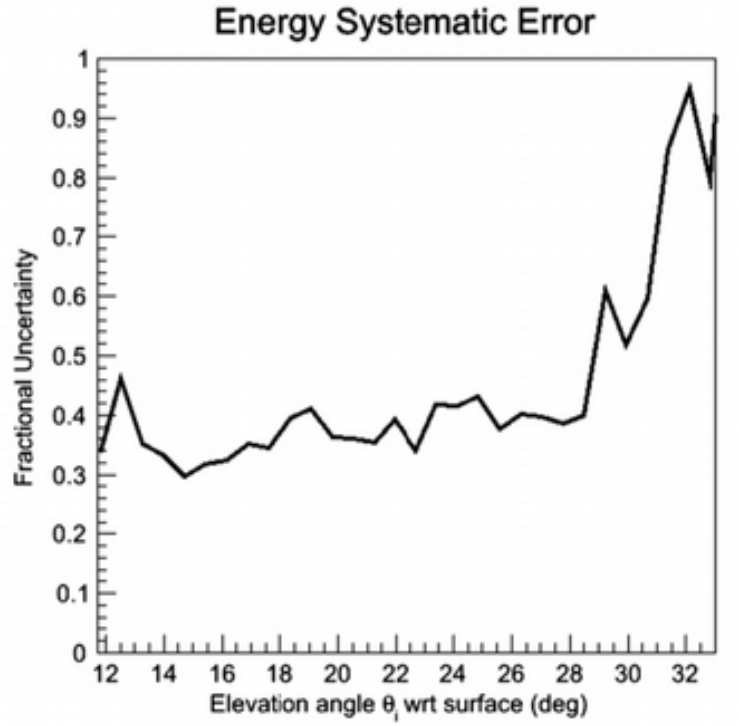

Figure 4.10: *The per-event fractional uncertainty of the CR reconstructed energy based on the solar reflection ratio analysis.*

4.2.3 Bistatic Radars

Bistatic radars are systems in which the transmitter and receivers are separated by some distance. In order to overcome some of the drawbacks of the previous measurements noted above, the HiCal experiment was proposed to function as the transmitter in a bistatic system with the ANITA payload acting as the receiver. HiCal was implemented as a payload carried on a separate balloon, launched in conjunction with the ANITA payload and maintained a varying separation distance during the flights allowing for signals transmitted from HiCal to be received by ANITA. This allowed the transmitted signal to be tailored to the ANITA frequency regime and provided direct, forward beamed reflection measurements of the Antarctic surface over a wide range of incidence angles and a wide range of surface reflection locations.

Chapter 5

HiCal-1: Design, Implementation, Performance

The first section of this chapter covers the external design constraints imposed on the development of the HiCal payload. The second section describes the design goals that we determined for the HiCal payload before and during the actual design and construction. Included here are motivations for each design point. The third section will provide a description of the HiCal-1 payload as it was constructed and where necessary includes explanations for constraints that prevented implementation of the desired design goal. The final section in this chapter is an assessment of the engineering performance of the HiCal-1 flight. The physics performance and data analysis are presented in the next chapter.

5.1 Design Constraints

The first iteration of HiCal did not have a dedicated budget, requiring the use of many inexpensive materials and methods. The HiCal flights are supported by Columbia Scientific Ballooning Facility (CSBF) and must meet certain size and weight requirements in order to be launched. The total payload weight (including the CSBF hardware used for tracking and communicating) has a limit of 12 lbs. The payload will be hand launched requiring that the number and size of compart-

ments in the payload chain be reasonable for one person to handle while walking or potentially running, as was the case in the HiCal-1a launch, see Fig. 5.1. Furthermore, the separation distance between HiCal and ANITA is not controllable during flight and the HiCal payload has no attitude control. The low priority of the payload and limited recovery support in Antarctica eliminates the possibility of retrieving the payload after the flight. This requires that all data be telemetered to a ground station during flight. Most payloads of this size supported by CSBF will have two separate telemetry units to transfer data, a 'high rate' and 'low rate' unit. Due to payload weight constraints and the additional hardware needed for HiCal, CSBF can only provide a 'low rate' data transfer (240 bytes/minute) for this process.

Figure 5.1: *The launch of the HiCal-1a payload is shown on the left and the full payload chain including the balloon shortly after launch is shown on the right. The launch is conducted by the CSBF rigging crew, Derek Dolbey is on the left releasing the payload, Joe Masters is pictured on the right. Photo credit to Brian Hill.*

5.2 Design Goals

5.2.1 Transmitter

Since our goal is to probe frequency dependent decoherence caused by surface roughness, the pulse frequency content would optimally be flat across the ANITA band (200-1200 MHz).

As the ANITA horn antennas are dual polarized and the surface features on the ice are often striated, it would be ideal for HiCal to have a dual polarized transmitter. This will allow event by event comparison between the two polarizations potentially providing insight into the orientation of the surface striations and a check for correlation with the prevailing local wind direction. This analysis would also require knowing the HiCal azimuth and attitude information at the time of each pulse transmission.

The transmitter beam pattern should be such that the signal directed toward ANITA and the signal directed toward the ground are identical. Since the payload has no attitude control, this removes the need to know the orientation of the HiCal transmitter during each transmission. It would also be acceptable if the beam pattern is sufficiently well characterized that the ground directed pulse can be determined by only knowing the ANITA directed pulse and the ANITA-HiCal separation distance. This requirement is necessary in order to determine the relative difference in power between the direct and reflected pulses received by ANITA.

5.2.2 Signal Strength

The separation between the HiCal and ANITA balloons will not be controllable during flight. The minimum achievable separation distance will largely be determined by timing of the HiCal launch window following the ANITA launch and maximum separation distance may be so long that HiCal and ANITA do not have line-of-sight between each other. In order to deal effectively with an unpredictable and varying separation distance, the pulsing and transmitting hardware should have a variable power output that is controllable from the ground during flight. This will ensure that the HiCal signal is reaching ANITA from long distances while not saturating the ANITA hardware at

short distances. Variation in separation distance is actually desirable since it will sample a wider range of reflection incidence angles. The best way to achieve this is to launch HiCal immediately following the ANITA launch, with the two payloads then gradually drifting apart.

5.2.3 Event Timing

The transmitted pulses should be synced to the pulse-per-second (PPS) output of an on-board GPS unit. This timing will provide the most straightforward case for identifying HiCal events in the ANITA data set. In the case where it is not possible to sync the pulses to the PPS, timing of the pulses should be recorded and transmitted to ground by the HiCal payload. In this case, it should still be possible to match HiCal events in the ANITA data by looking at the relative time separations between events as recorded on the two payloads. As a worst case scenario, the HiCal events in the ANITA data set should be identifiable even if only the locations of the two payloads are known using the interferometric reconstruction. Reflected events would then be identifiable knowing the difference in time-of-flight between the direct and reflected events, which can be determined with the payload positions and surface elevation at the point of reflection.

5.2.4 In-flight Monitoring and Control

The CSBF ground crew should have command control over turning the pulse transmission on and off and have live monitoring of the science data, motor battery voltage, and position.

5.3 HiCal-1

5.3.1 Payload Hardware, Software, and Data Format

HiCal-1 consists of five main components: 1) Micro-Instrumentation Package (MIP) provided by CSBF, 2) pulse timing board, 3) pulsing unit 4) transmitting antenna and 5) batteries. These components are contained in two separate housings, the instrument box (MIP, timing board, and batteries)

and the pressure vessel (pulsing unit and antenna). The in-flight configuration of all components is shown in Figure 5.2. The flight-ready payload is shown in Figure 5.3. The instrument box is a 9"x5"x6" powdercoated aluminum box. Two GPS antennas, an Iridium communication antenna, and a pulse pickup antenna are attached to the outside of the payload box by SMA bulkhead connectors. The high voltage components are contained in a separate pressure vessel housing constructed of ABS plastic. ABS was chosen over the more common PVC plastic because it is more resistant to degradation under UV exposure. The pressure vessel is necessary since the breakdown distance at kV amplitudes and the reduced pressure experienced at float cause unwanted arcing across the dipole and leads of the piezo element. A photodiode array was intended to serve as a sun-sensor and was initially included in the payload, hanging vertically below the pressure vessel, but ultimately did not fly due to concerns about the total payload weight. A more detailed description of the main components is as follows:

The MIP is the data processing board which handles all communications, data transmission and positional GPS data. This board is provided by CSBF and is the standard used for all of their smaller, hand-launched payloads. The timing board was developed by the University of Kansas Instrumentation Design Lab (IDL) to process and packetize the science data before sending it to the MIP for transmission to the ground station. The timing board receives time-of-day (TOD) and pulse-per-second (PPS) from a dedicated GPS antenna, and a high-voltage pulse, HVP, from the pickup antenna whenever the HiCal transmitter issues an RF signal. The HVP is passed through a protection circuit that limits the voltage sent to the complex programmable logic device (CPLD). A high speed counter on the CPLD is gated by incoming PPSs and HVPs. The CPLD receives a PPS signal from the GPS and begins a sub-second count until it receives the HVP. Once this occurs, the GPS TOD associated with the most recently received PPS and sub-second count are combined as the event time-stamp. The sub-second count is accurate down to approximately 20 ns. The timing board can store up to 14 events at once in a 'science packet' that is sent to the MIP upon request. The rate that the MIP requests packets (fastest at 1 packet/min) is commandable and can be changed during flight.

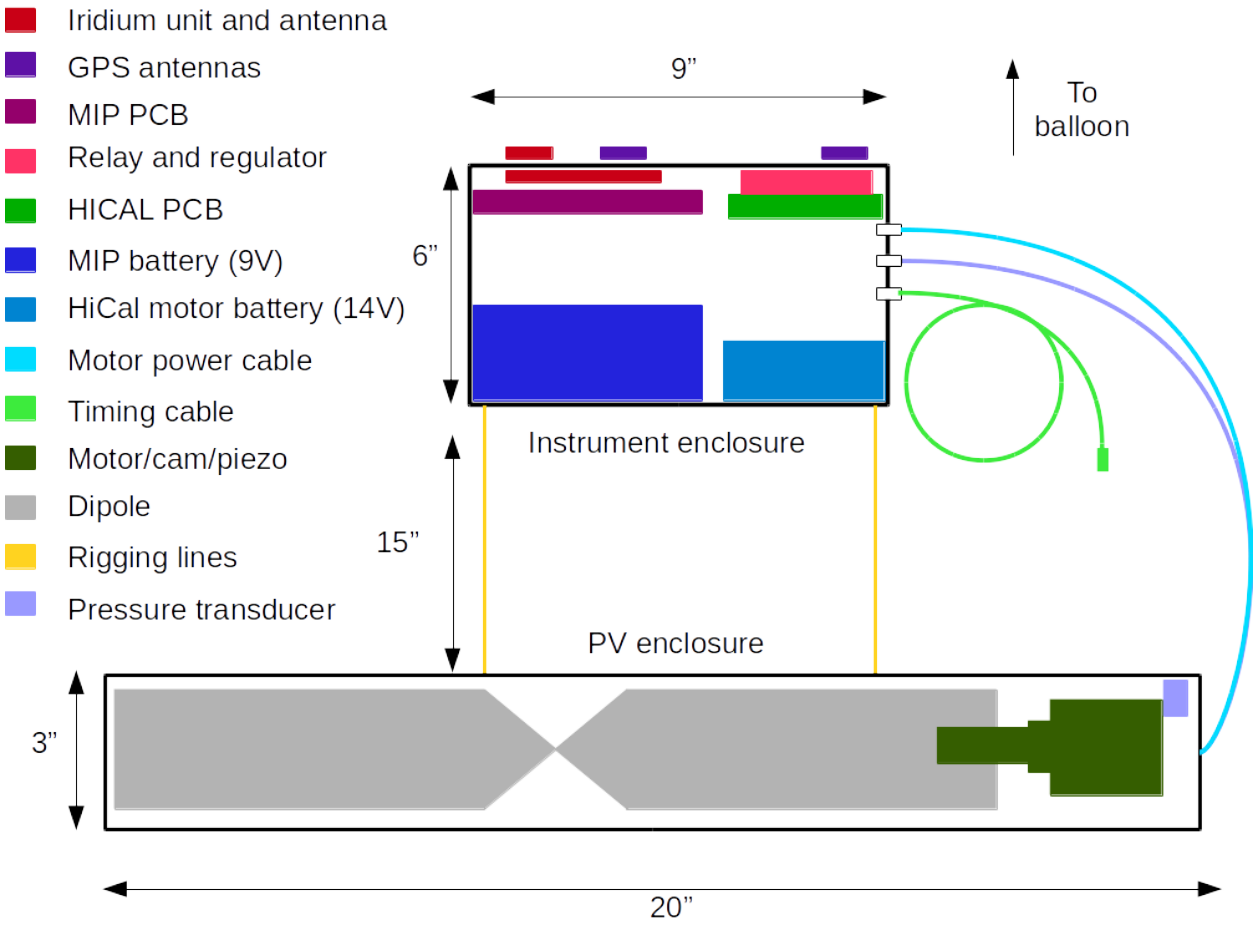

Figure 5.2: *The layout and components of the HiCal-1 payload are shown. The top compartment, the instrument enclosure, houses all of the data and communication electronics as well as the batteries. The lower compartment is a pressure vessel which houses all of the high-voltage components including the piezo generator and the transmitting antenna.*

Figure 5.3: *Photo showing the flight-ready HiCal-1 payload.*

The pulse is produced by an off-the-shelf grill igniter containing a spring and hammer system that strikes a piezo crystal outputting up to 5 kV to the transmitting antenna. Several different sparking methods were evaluated and the grill igniter was chosen for having the highest bandwidth. A comparison of the frequency content of pulses from the various sparking methods are shown in Fig. 5.4. Fig. 5.5 shows the assembled pulsing unit and the transmitting antenna with and without a stabilizing sleeve. A 12 V DC motor turns a helical cam that compresses the button of the igniter. With a 12 V supply the cam rotates at 0.3 Hz (20 RPM).The transmitting antenna is an aluminum dipole originally developed for the RICE experiment [33], 180-1200 MHz, oriented horizontally during flight.

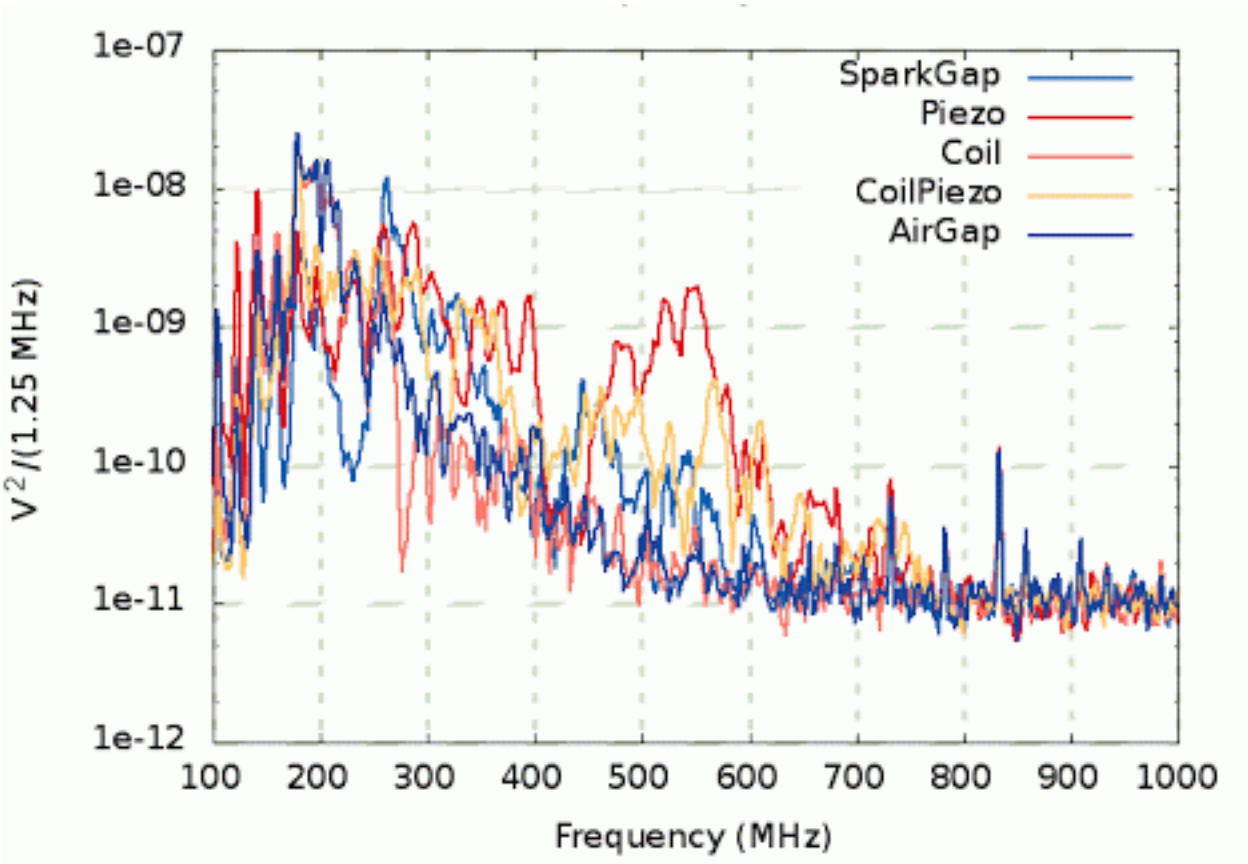

Figure 5.4: *Comparison of frequency output from various sparking methods.*

The pressure vessel is constructed from four pieces of ABS plastic: a tube 23" long with 4.5" OD and 3.998" ID, a thread-less female end cap, an open threadless flange, and a flat end cap that covers the flange. The female end cap is permanently attached to one end of the tube using an ABS

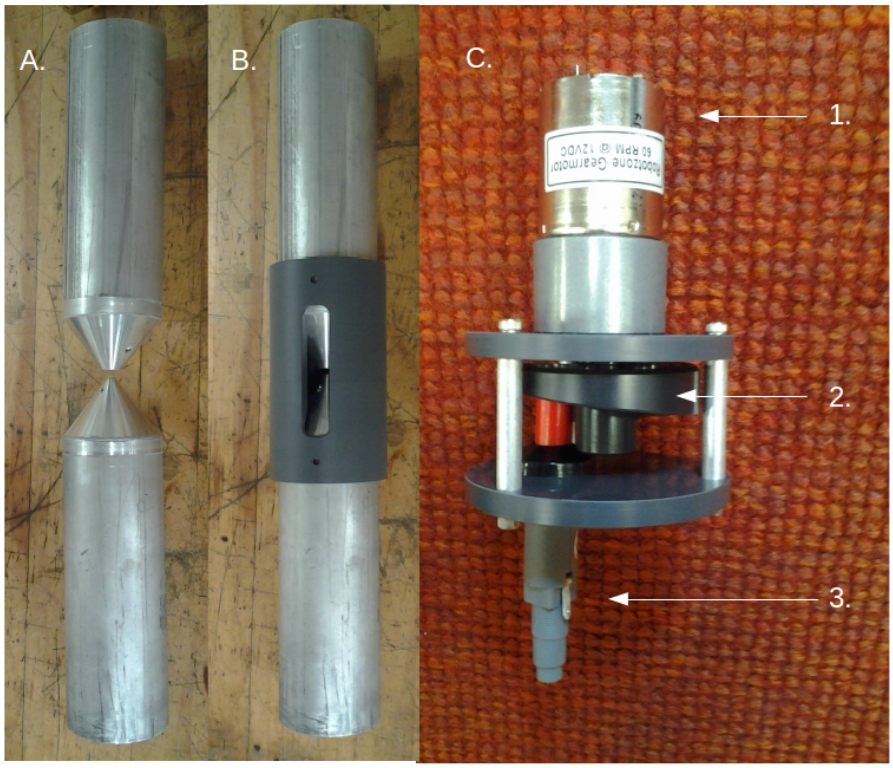

Figure 5.5: *Main components of the transmitting unit. A) Transmitting dipole antenna shown A) without and B) with a support collar. C) The spark generator showing the 1) DC motor, 2) helical cam and 3) off the shelf piezo sparker. As the cam rotates, the red button of the sparker is depressed, causing a spring-mounted mass to release and impact the piezo element. The voltage potential is created across two leads protruding from the bottom of the sparker casing. Each of these leads is connected to one 'side' of a coaxial cable which is then connected to each of the sides of the dipole at the center feedpoint.*

epoxy. The flange is similarly attached to the other end of the tube. The flange and flat cap are drilled with 8 matching holes and are secured together using stainless steel bolts and nuts. The flat cap additionally has a circular groove cut on the inner side where a greased O-ring will be secured in order to create an airtight seal between the flange and cap. Fig. 5.6 shows the inner side of the end cap. Wires for the motor and pressure transducer power and the pressure transducer output are passed through a hermetically sealed connector in the flat end cap.

An example of a science packet is shown in Figure 5.7. The first line of the packet is a header, the next lines (up to 14) contain the event information and the final line is a termination signal to the MIP indicating end of transmission. The header contains a transmission number and the number of events recorded in the packet. Each event line contains the GPS second (4 bytes), sub-second (4 bytes), and photodiode readouts (8 bytes).

5.4 HiCal-1 Engineering Performance

During the 2014-15 Antarctic balloon campaign, two HiCal launches were completed with one successful flight. HiCal-1a was launched two days after the ANITA-3 launch. Science packets were received for the first hour of the flight, ending when the payload was at an altitude of 5 km. Using a ground station consisting of an ANITA horn antenna and front end electronics (filters and high gain amp), we were able to detect weak and ragged pulses from the HiCal payload and believe the issue to be a cracked piezo element based on similar observations during ground tests that were confirmed by dissection of the faulty sparking unit. The HiCal-1a motor was then turned off for the remainder of its flight. HiCal-1b was launched after ANITA-3 had made a full revolution around the continent and passed to within 500 km of McMurdo station. The flight paths of ANITA-3 and HiCal-1b are shown in Figure 5.8. The HiCal-1b motor was turned on for a total of approximately 14 hrs over the course of its flight. At a 3 Hz pulse rate, this should have resulted in 16-17,000 transmitted pulses. The HiCal-1b payload telemetered 3444 events.

Temperature variations during flight caused small variations in the battery voltage resulting in

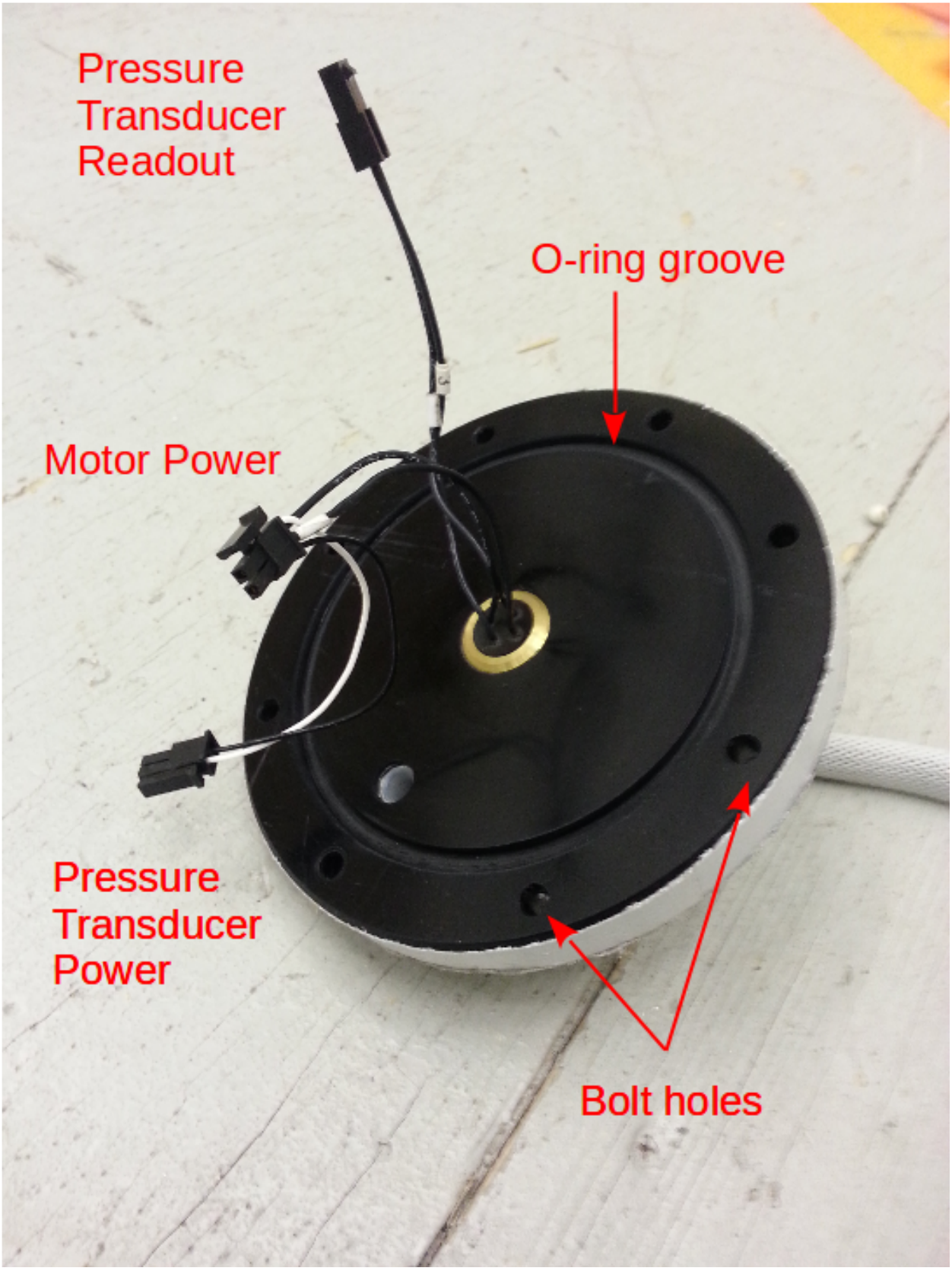

Figure 5.6: *Photo of the flanged endcap showing the hermeticly sealed electrical feedthrough, the electrical connections inside the PV, the o-ring groove and the eight bolt holes around the perimeter.*

```
10 53 E5 04 04 02 1E 0E
04 08 54 54 18 88 1C 02 A5 30 2D 30 2A 2A 2A 97  1414793220 35424280 2.12065936
06 08 54 54 79 C0 B4 02 A5 30 2D 30 2A 2A 2A 97  1414793222 45400185 2.09975905
08 08 54 54 F3 6F C2 02 A5 30 2D 30 2A 2A 2A 97  1414793224 46297075 2.00896890
0A 08 54 54 6A 14 9A 02 A5 30 2D 30 2A 2A 2A 97  1414793226 43652202 1.97355127
0C 08 54 54 1C E9 7F 03 A4 30 2D 30 2A 2A 2A 97  1414793228 58714396 2.15062194
0E 08 54 54 BB 97 4C 04 A5 30 2D 30 2A 2A 2A 97  1414793230 72128443 2.13414047
10 08 54 54 B6 E9 5F 05 A5 30 2D 30 2A 2A 2A 97  1414793232 90171830 2.18043387
13 08 54 54 1D D2 66 00 A5 30 2D 30 2A 2A 2A 97  1414793235 06738461 2.16566631
15 08 54 54 FF A5 2B 00 A5 30 2D 30 2A 2A 2A 97  1414793237 02860543 1.96122082
17 08 54 54 2A DC 88 00 A4 30 2D 30 2A 2A 2A 97  1414793239 08969258 2.06108715
19 08 54 54 E4 1C 25 01 A5 30 2D 30 2A 2A 2A 97  1414793241 19209444 2.10240186
1B 08 54 54 1A EE 7D 01 A5 30 2D 30 2A 2A 2A 97  1414793243 25030170 2.05820726
1D 08 54 54 CD 0F A7 01 A5 30 2D 30 2A 2A 2A 97  1414793245 27725773 2.02695603
1F 08 54 54 CF 6F D5 01 A5 30 2D 30 2A 2A 2A 97  1414793247 30765007 2.03039234
03
```

Figure 5.7: *An example of a science packet recorded and sent from the HiCal payload. Details of the format are in the text.*

variations of the motor RPM and pulse rate. During the HiCal-1b flight the motor speed ranged from 19.6 to 21.4 RPM. Due to the desired pulsing rate of the transmitter (20 events/minute) and the maximum data transfer rate allowed by the MIP (14 events/minute), under ideal operating conditions the number of event timestamps received on the ground will be 30 % lower than the number of events occurring. In addition, MIP housekeeping packets are transferred over the same Iridium feed as the science packets and the MIP will also only store one science packet at a time so if a science packet is not able to be sent before the next one is requested, the older packet is written over and lost. Since the science packet request rate is controllable during flight the housekeeping packet rate was kept at a 5 or 10 minute interval to decrease the number of lost science packets except during ascent when the rate was at 1 packet/min as required by CSBF for monitoring reasons. In addition to the loss of entire packets, many of the received science packets contained fewer than 14 events and were sometimes empty. It is not possible to determine with the HiCal data alone if these 'missing' events were the result of pulses that were successfully transmitted but not recorded or due to issues with the pulsing unit that resulted in no transmitted signal. The number of events per packet did not seem to be correlated to environment temperature or motor-on duration as shown in Figure 5.9.

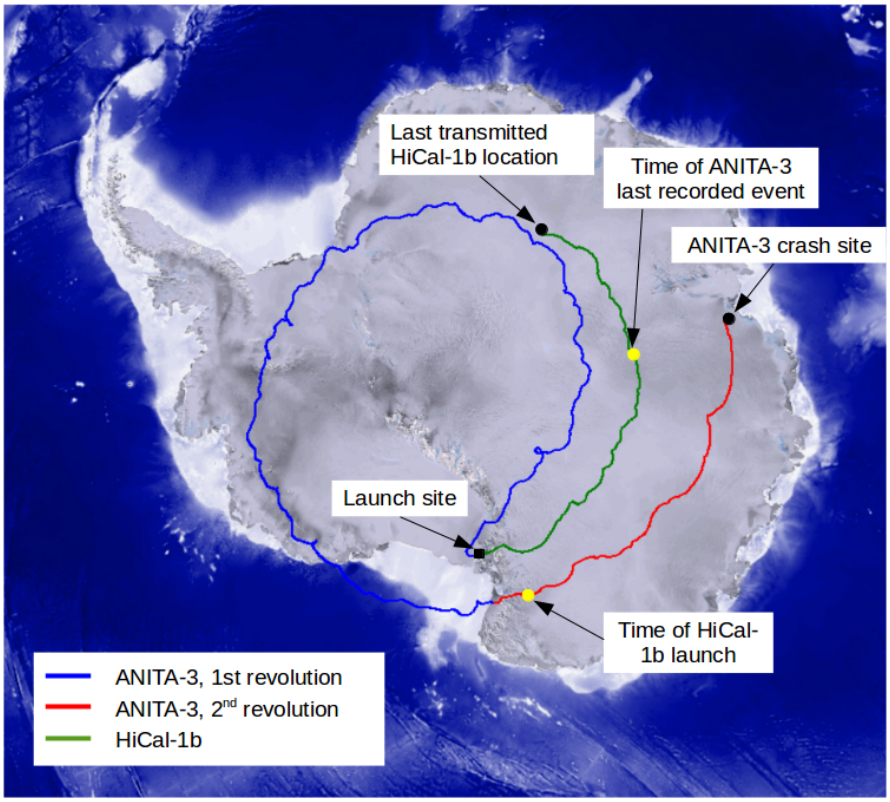

Figure 5.8: *The flight paths of ANITA-3 and HiCal-1b are shown, along with the location of the launches (the LDB, near McMurdo Station), the location of ANITA-3 when HiCal-1b launched, the location of HiCal-1b when the ANITA-3 DAQ was turned off, the location of the ANITA-3 crash site and location of HiCal-1b when communication with the payload was lost due to drop in battery voltage.*

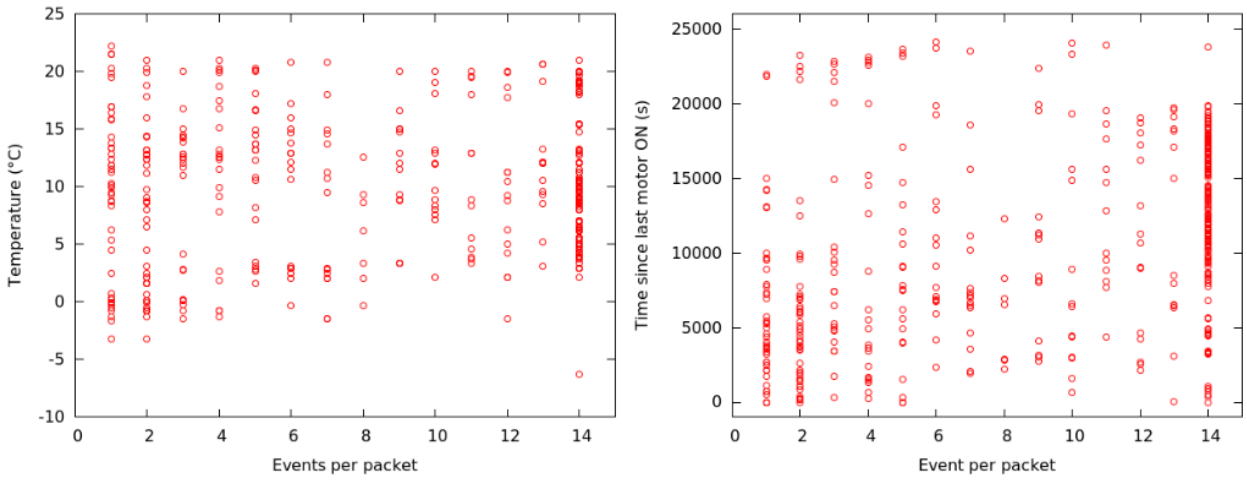

Figure 5.9: *Number of events recorded per packet in relation to external atmospheric temperature for periods of time when HiCal motor was on.*

There was a significant issue with the HiCal recorded event timestamps that was not resolved before the flights. An example of this issue is displayed in Fig. 5.10. While the sub-second times are believed to be accurate to within 20 ns, the GPS seconds recorded are not self-consistent having subsequent events with earlier timestamps than previous events. The cause of this issue has not been determined but after studying the list of event timestamps in hexadecimal format, it became obvious that there was a (seemingly) randomly occurring shift of 1 or 2 digits in the 16^2 position of the number resulting in a backward jump in time of 256 or 512 seconds. By adjusting these shifts, it is possible to make the entire set of timestamps be self-consistent. However, without further analysis it is not possible to determine if the timestamps are absolutely correct or still only relatively correct. This is discussed further in the following analysis section.

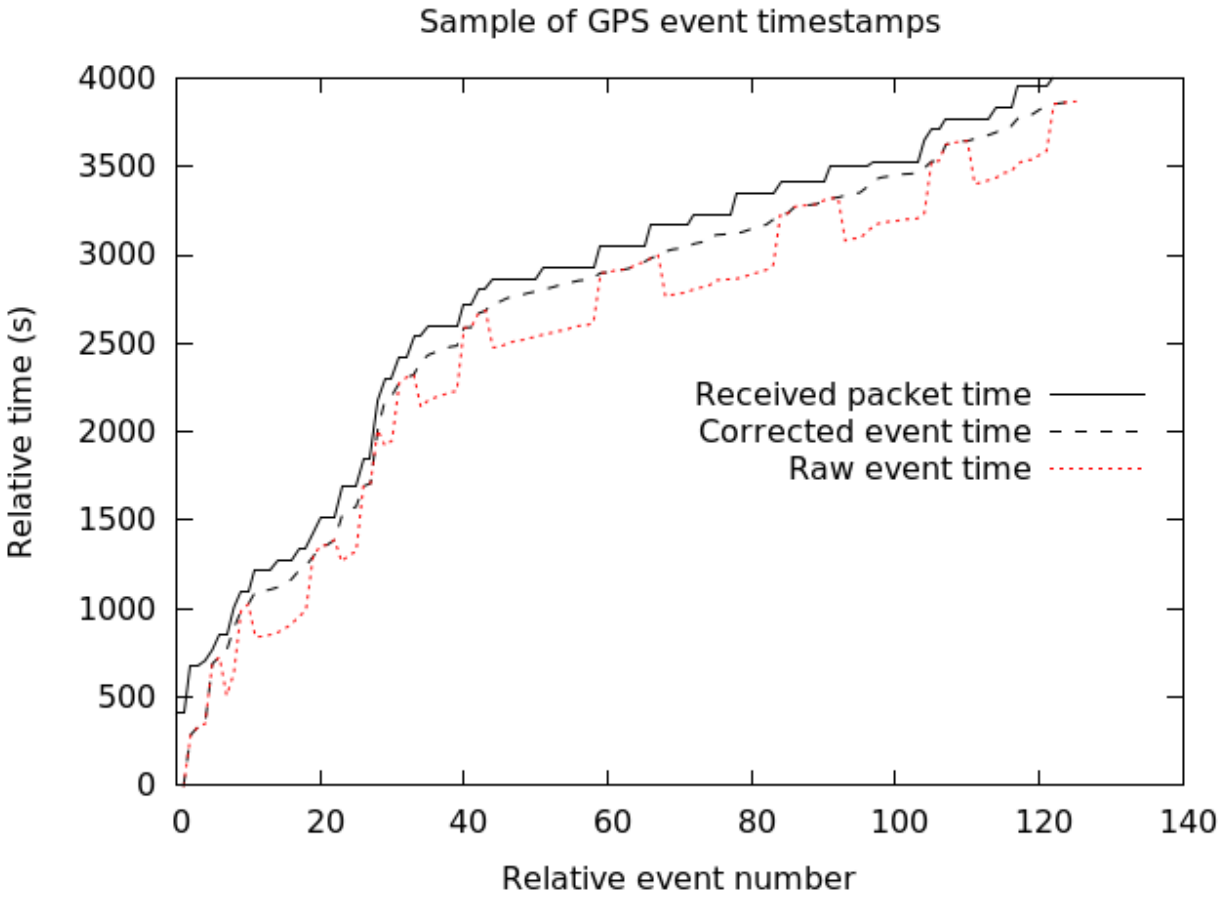

Figure 5.10: *Arbitrary range of HiCal-1 timestamps showing the issue with the raw data and the corrected timestamps in relation to the time when packets were received by the ground station.*

Chapter 6

HiCal-1 and ANITA-III Analysis

6.1 Identifying HiCal Pulses in ANITA Data

Of the 3444 timestamps recorded by the HiCal-1 payload, it was initially not possible to match any of the timestamps with timestamps in the ANITA-3 data when accounting for travel time of the signal between payloads because of the issue discussed at the end of the previous chapter. Consequently, two other methods were first used to identify HiCal events in the ANITA data set. These methods, 'dt identification' and 'template identification', are described in detail in the following subsections. Both of these methods require knowing the relative positions of the two payloads in order to determine pointing directions between the payloads and differences in time-of-flight (TOF) for the reflected and direct signals, so first I will go over the geometry and necessary calculations.

Fig. 6.1 provides a diagram with the distances and angles corresponding to the two payloads that are necessary for determining the TOF and pointing directions for signals from HiCal to ANITA. The azimuthal angle from ANITA to HiCal, ϕ_{AH} with respect to North, is given by Eq. 6.1 and only depends on the GPS coordinates of the two payloads. The elevation angle from ANITA to HiCal, with respect to ANITA's horizontal, is given by Eq. 6.2. This is dependent on the locations and altitudes of the payloads which are used to determine the separation distance, d_{HA}, and separation angle, θ_{HA}, from which ϕ_{AH} can be determined geometrically. The location (and thus angles

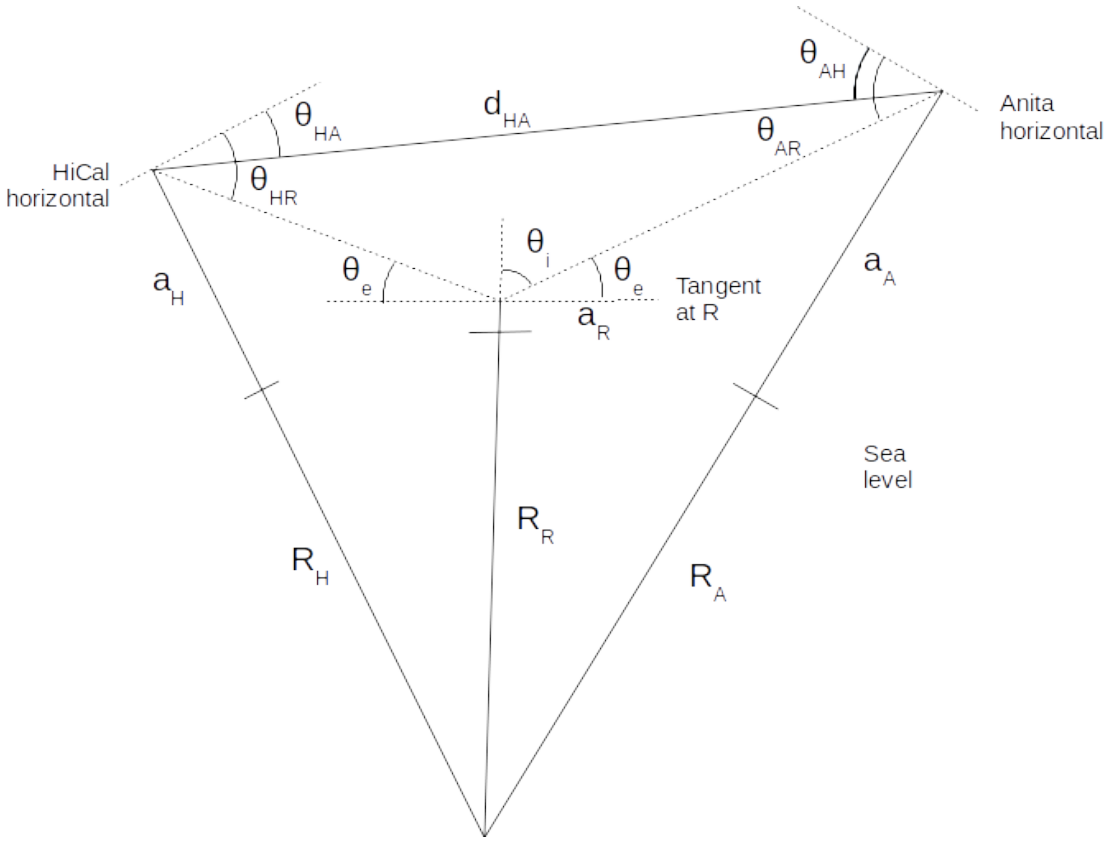

Figure 6.1: *Payload altitudes, a_H and a_A, are from sea level and reflection point altitude, a_R, denotes the ice surface. Earth radii, R_H and R_A, are from earth center to sea level. Angles which are not shown: azimuthal angle from HiCal to reflection point and HiCal to ANITA $\phi_{HR} = \phi_{HA}$ and asimuthal angle from ANITA to reflection point and ANITA to HiCal $\phi_{AR} = \phi_{AH}$*

to) the reflection point has to be determined numerically due to the non-functional shape of the ice-sheet surface. This is done iteratively by scanning over surface points in the HiCal-ANITA-Earth center plane for the location where incidence angles toward each payload are equal. The WGS-84 Geoid and Radarsat Antarctic Mapping Project Digital Elevation Model (RAMPDEM, ver 2) [48] are used for sea-level and ice sheet elevations, respectively.

$$\phi_{AH} = tan^{-1}\left(\frac{sin(\lambda_H - \lambda_A)cos(\phi_H)}{cos(\phi_A)sin(\phi_H) - sin(\phi_A)cos(\phi_H)cos(\lambda_H - \lambda_A)}\right) \tag{6.1}$$

$$\theta_H = \frac{\pi}{2} - sin^{-1}\left(\frac{a_H + R_H}{d_{HA}sin(\theta_E)}\right) \tag{6.2}$$

The azimuthal angle from ANITA to the reflection point is assumed to be the same as ϕ_{AH}. The elevation angle from ANITA to the reflection point, θ_R, cannot be solved for analytically since it depends on the surface elevation of the ice sheet. An iterative process was developed to determine the GPS location of the reflection point by requiring the elevation angles, θ_e, for an incoming (from HiCal) and outgoing (to ANITA) ray be equal.

The ANITA-3 position is updated once every second. The HiCal-1 position is updated much less regularly since the GPS signal was only recorded in the house-keeping packets as discussed in the previous chapter. To streamline the data processing, the HiCal-1 position data was interpolated to 1 second increments and paired with the ANITA-3 positions. Prior to looking for HiCal events in the ANITA data, a rootfile was produced to serve as a lookup table providing bearing angles, separation distances and times-of-flight for the HiCal and reflection point locations for every second that HiCal was pulsing.

6.1.1 dt Identification

From the individual TOFs for the direct and reflected signals, expected time differences, Δt_{exp}, are determined over the course of the flight. The time differences between successive ANITA event triggers, Δt_A, were analyzed against Δt_{exp}. If $\Delta t_A = \Delta t_{exp}$, the two corresponding ANITA events are

marked as a direct and reflected pair. Figure 6.2 shows Δt_{exp} and incidence angles over the course of the HiCal-1b flight.

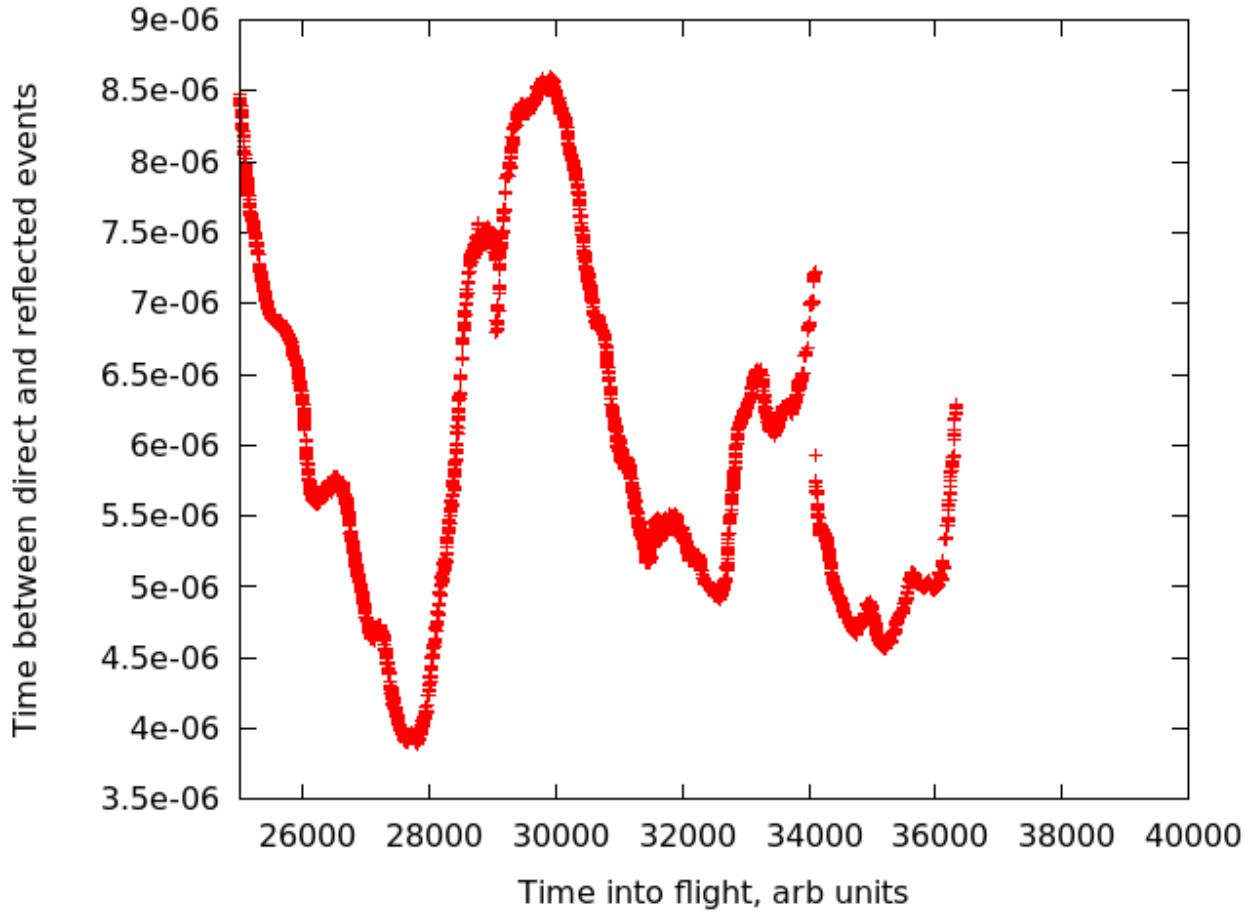

Figure 6.2: *Variation of arrival time separation between direct and reflected events over the course of the HiCal-1b flight.*

Using these Δt_{exp} values, a search was performed over the ANITA-3 data that coincided with HiCal-1 flight times looking for pairs of subsequent events with timestamp separation Δt_A matching the calculated Δt_{exp} at that given time in the flight. This search resulted in a set of 100 R and D pairs.

6.1.2 Template Matching Identification

Since the number of paired events was lower than anticipated, another search in the ANITA-3 data set was performed using the pointing direction from ANITA to HiCal as a first cut. In each

ANITA-III event interferogram, a peak in intensity co-located with the pointing direction to HiCal-1 identifies that event as a possible HiCal-1 event. The initial search was done with a $\pm 10^{\circ}$ cut in elevation and a $\pm 5^{\circ}$ cut in azimuth. The larger elevation angle window was used to include the area on the ground where reflected events were anticipated.

From the list of events that passed the pointing cut, there is still a large number of non-HiCal events. A narrower pointing cut, peak voltage cut, and timing cut would be sufficient for removing the non-HiCal events, but differences in the ANITA background and HiCal behavior between runs would require tuning the cut bounds by hand for each run. Figures 6.3, 6.4, and 6.5 show each of these variables for two runs, demonstrating the variability in behavior.

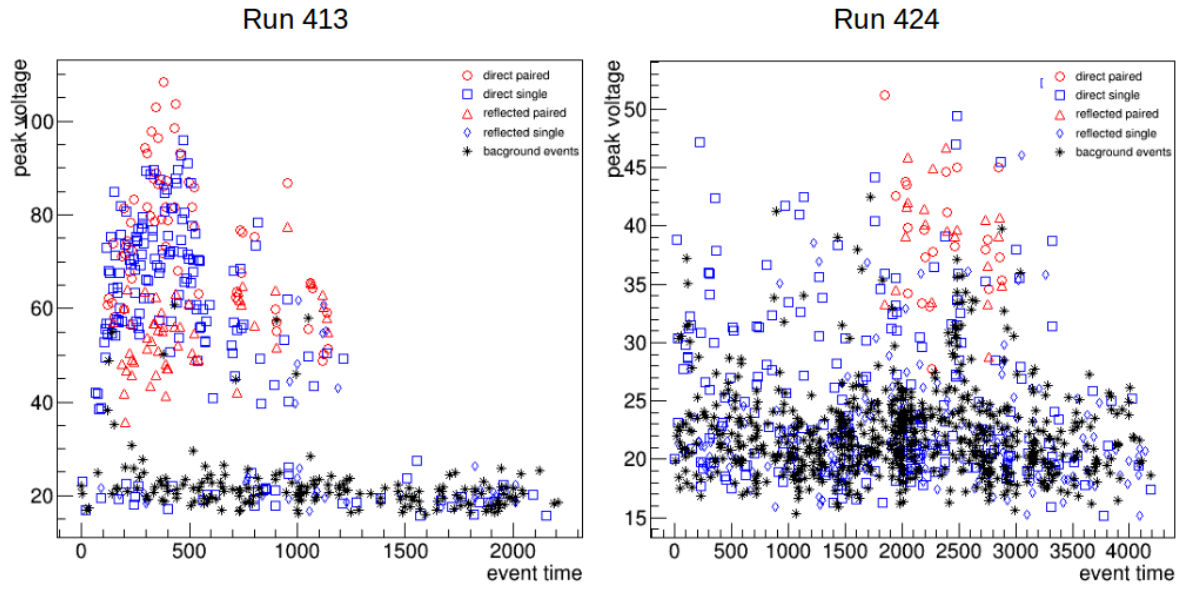

Figure 6.3: *Both frames show all events from the initial pointing cut. Run 413, on the left shows a clear separation in peak voltage between the HiCal and non-HiCal events. Run 424, on the right, does not.*

In order to quantitatively and indiscriminately identify the HiCal events from the pointing cut event list, a waveform template matching technique was employed. Each new event is cross-correlated with all current templates and is paired with the template for which it has the highest cross correlation value (CCV). The new event is then added and averaged into the highest-matched template. It is also required that an event point to the same location as the other events in the

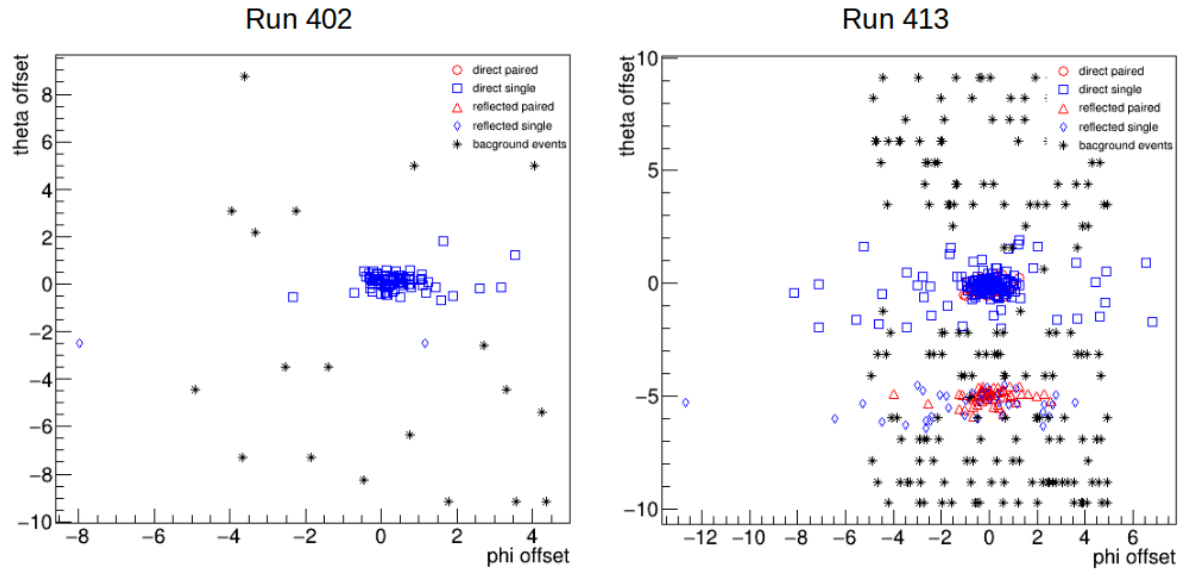

Figure 6.4: *Both frames show all events from the initial pointing cut. Run 413, on the left shows a clear separation in peak voltage between the HiCal and non-HiCal events. Run 424, on the right, does not.*

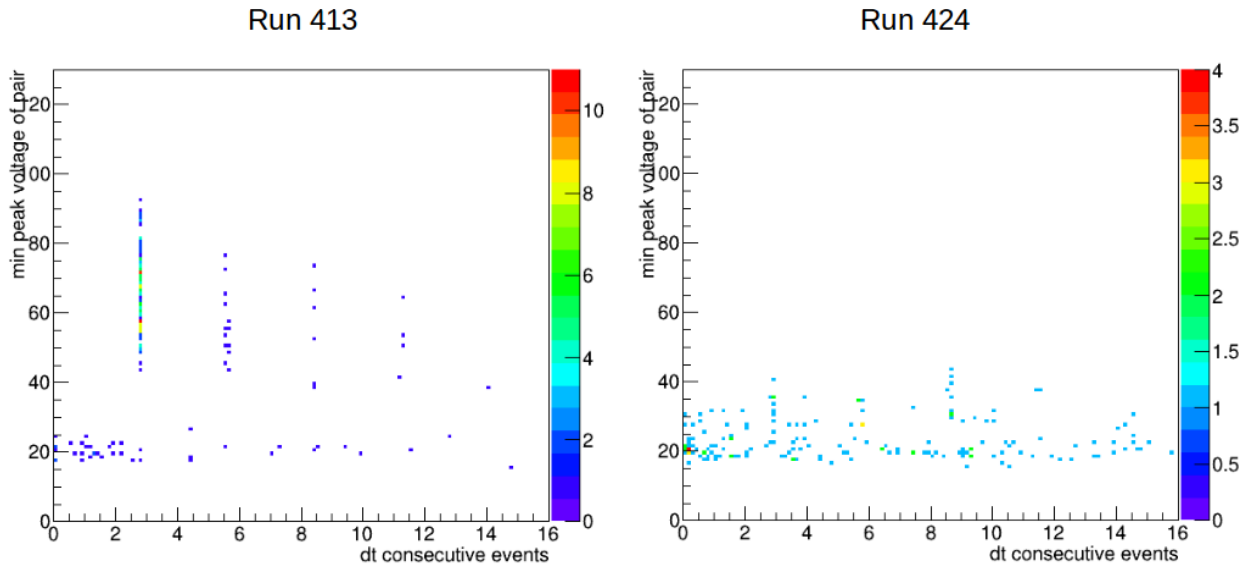

Figure 6.5: *Both frames show all events from the initial pointing cut. Run 413, on the left shows a clear separation in peak voltage between the HiCal and non-HiCal events. Run 424, on the right, does not.*

highest-matched template. This is done largely to have separate templates for the direct and reflected events. A new template is made whenever an event is not highly correlated with a previous template and has an SNR value above a cut set to discriminate between interesting and non-interesting events.

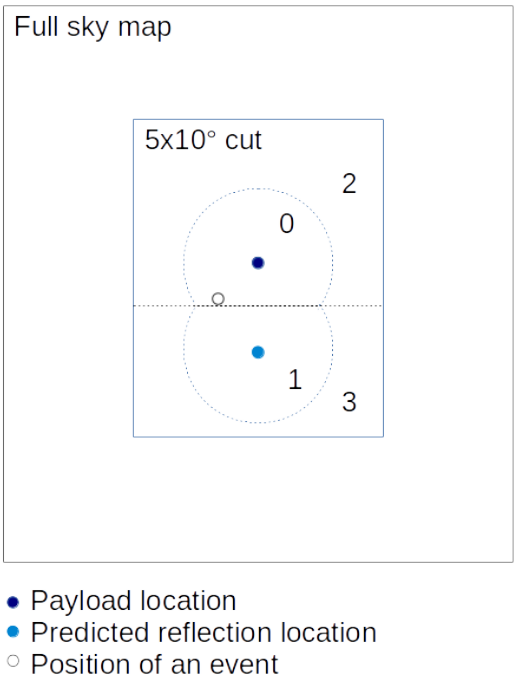

Figure 6.6: *Shown are the bounds for the cut areas. The initial pointing cut area is subdivided into four smaller regions that are used to group events into four possible template locations. (0) is 'close to HiCal direct' (1) is 'close to HiCal reflected' (2) is 'not close to either but closer to HiCal direct' (3) is 'not close to either but closer to HiCal reflected'.*

Figure 6.8 shows CCV between all events in run 413 and the final result of template (A). Region (A) in this plot contains only events that originally matched with templates (A) and (B). We do not expect to see any HiCal events in box (C) of Figure 6.8. If there are HiCal events here, we would expect the 'on' distribution to be more dissimilar to the 'off' distribution. Shown in Figure 6.9, the similarities of these two populations, especially at lower fdPhi, indicate that there

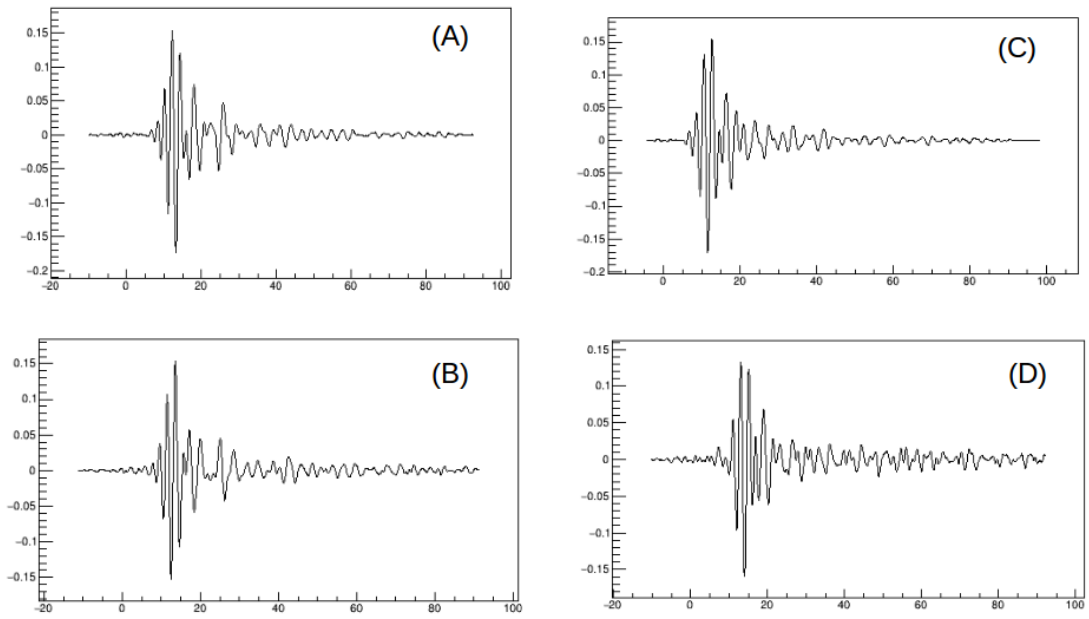

Figure 6.7: *Four examples of final templates. (A) run 413 region (0), (B) run 413 region (1), (C) run 421 region (0), (D) run 421 region (1). To force separate templates being made for direct and reflected events, events are only checked for correlation with templates containing other events in the same area. For example, a new event pointing to region (1) in run 413 would only be checked for correlation agains template (B).*

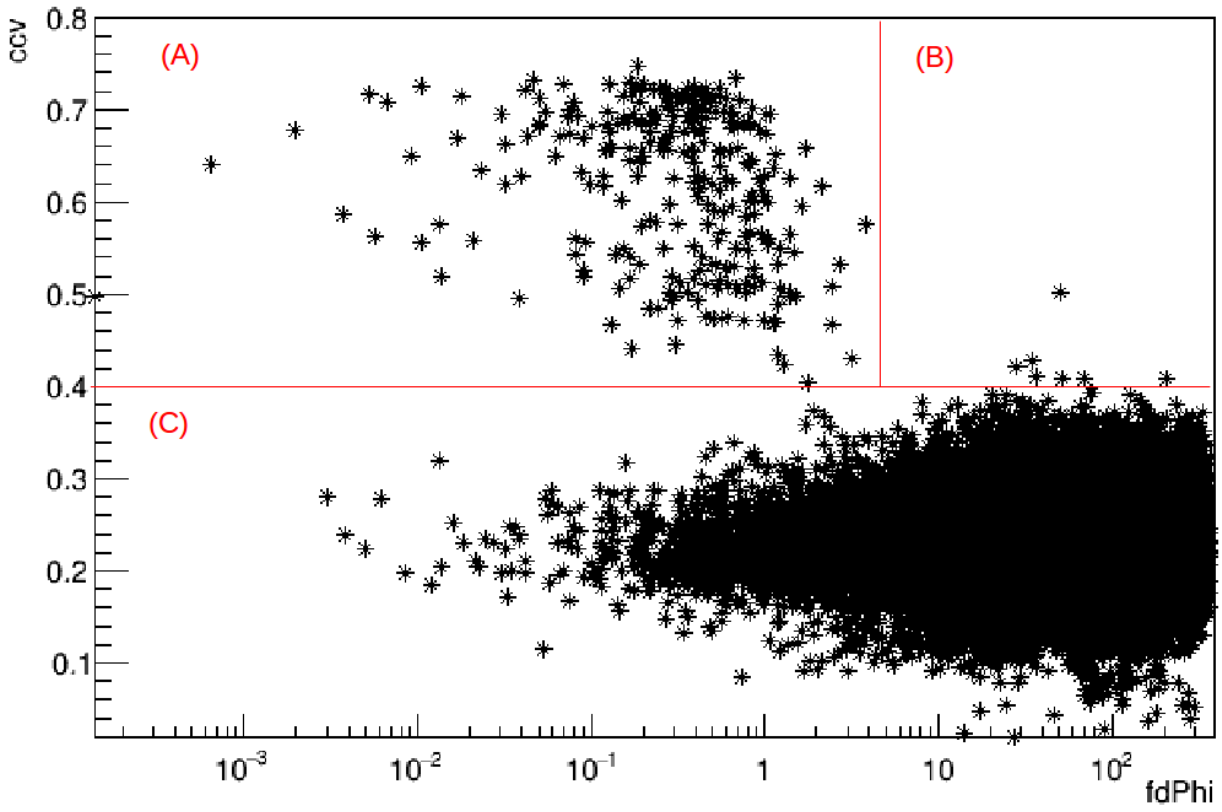

Figure 6.8: *Cross correlation values (ccv) and pointing offset in ϕ (fdphi) plotted for all events in run 413. CCV values are from each event and template (A) shown in Figure 6.7. Region (A) contains all events that were included in templates (A) and (B) from Figure 6.7 and no events that were not. Region (B) contains events that correlated highly with the template but did not meet pointing cuts and occurred when the HiCal motor was off. Events in region (C) are detailed in Figure 6.9*

.

is not a population of missed HiCal events at lower CCV.

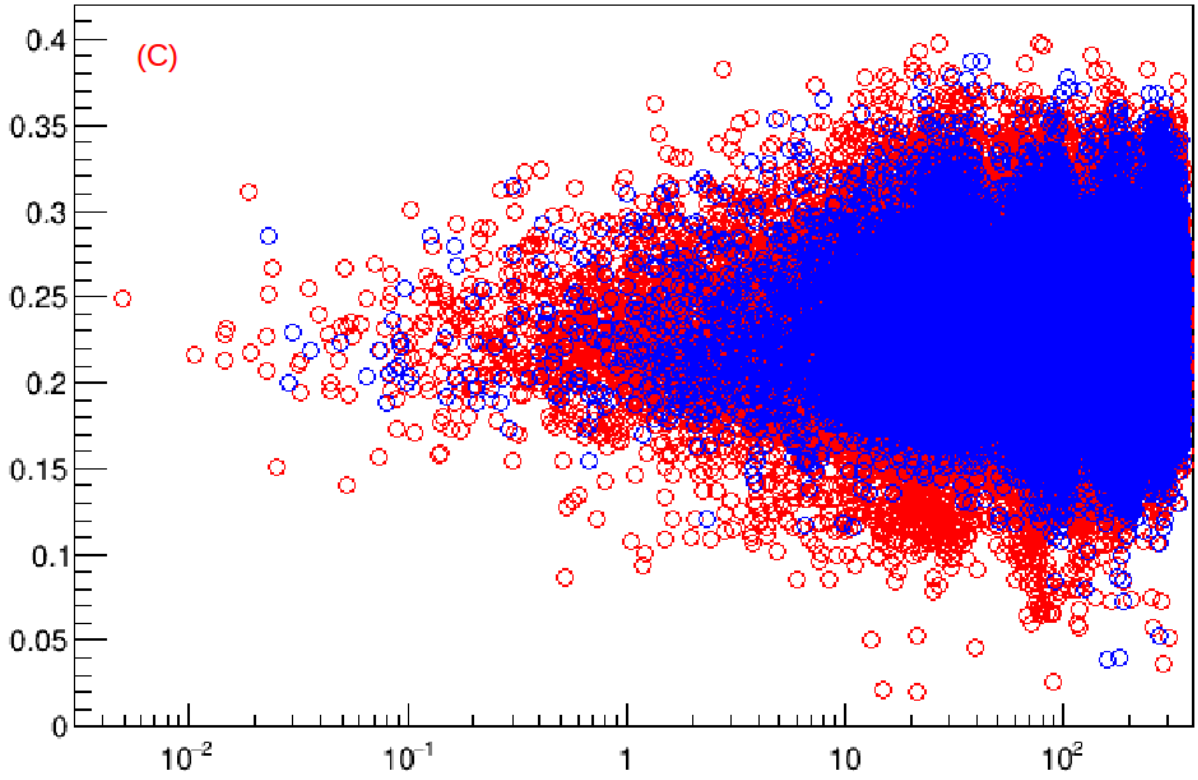

Figure 6.9: *Events from region (C) in Figure 6.8 divided into when the HiCal motor was on (blue) and off (red). The similarity of these two distributions would indicate that there are not HiCal occuring when the motor was powered off.*

6.1.3 Timestamp Matching Identification

Following the completion of the template matching procedure, the event statistics were high enough to determine that the initial timestamp matching attempt had produced no results because the HiCal GPS and ANITA GPS seconds were offset by 2.25-2.55 ms. With this information, the timestamp matching was redone and resulted in identifying an additional 118 events that were not included in the template matching results.

6.2 Paired and Unpaired HiCal Events

In order to determine reflection coefficients from the set of HiCal events it is necessary to understand why there were unpaired events. This is due to the possibility that some reflected events were not recorded because the surface effects caused a reduction in the reflected signal amplitude that prevented the reflected event from passing the ANITA trigger. If this occurred for any significant number of events, the reflection coefficients calculated from the paired events would be biased higher than if the missing events were included. To determine if this is an issue, we have to determine why there were missing reflected events. It is possible that a HiCal event would not be recorded by ANITA if 1) the payload was detecting another event, 2) experiencing dead time during the writing of events to disk, or 3) the reflected event did not trigger. The first case can be checked directly by checking timestamps of the events following or preceding an unpaired event. The second case can not be checked directly on an event by event basis but requires using a measure of the ANITA efficiency. If the first two cases are ruled out, it will be necessary to determine if the cause for case 3 is a transmission effect or a surface effect.

6.2.1 Interfering Events

For case 1) above, it is possible to determine events were missed simply by looking for events detected within a certain time period, dt, following a direct event or preceding a reflected event. For an unpaired direct event, $dt = t_{next} - t_{direct}$ and for an unpaired reflected event, $dt = t_{reflected} - t_{previous}$. The length of a recorded ANITA-3 event is 100 ns and separation between successive events is as small as 250 ns. So if the measured dt for an unpaired event is within 350 ns of the predicted paired dt, it is possible that the missing event occurred but was not recorded. As an example, Figure 6.10 shows dt for a single run. All runs with HiCal events had the same results showing that there are not missing HiCal events due to interfering events.

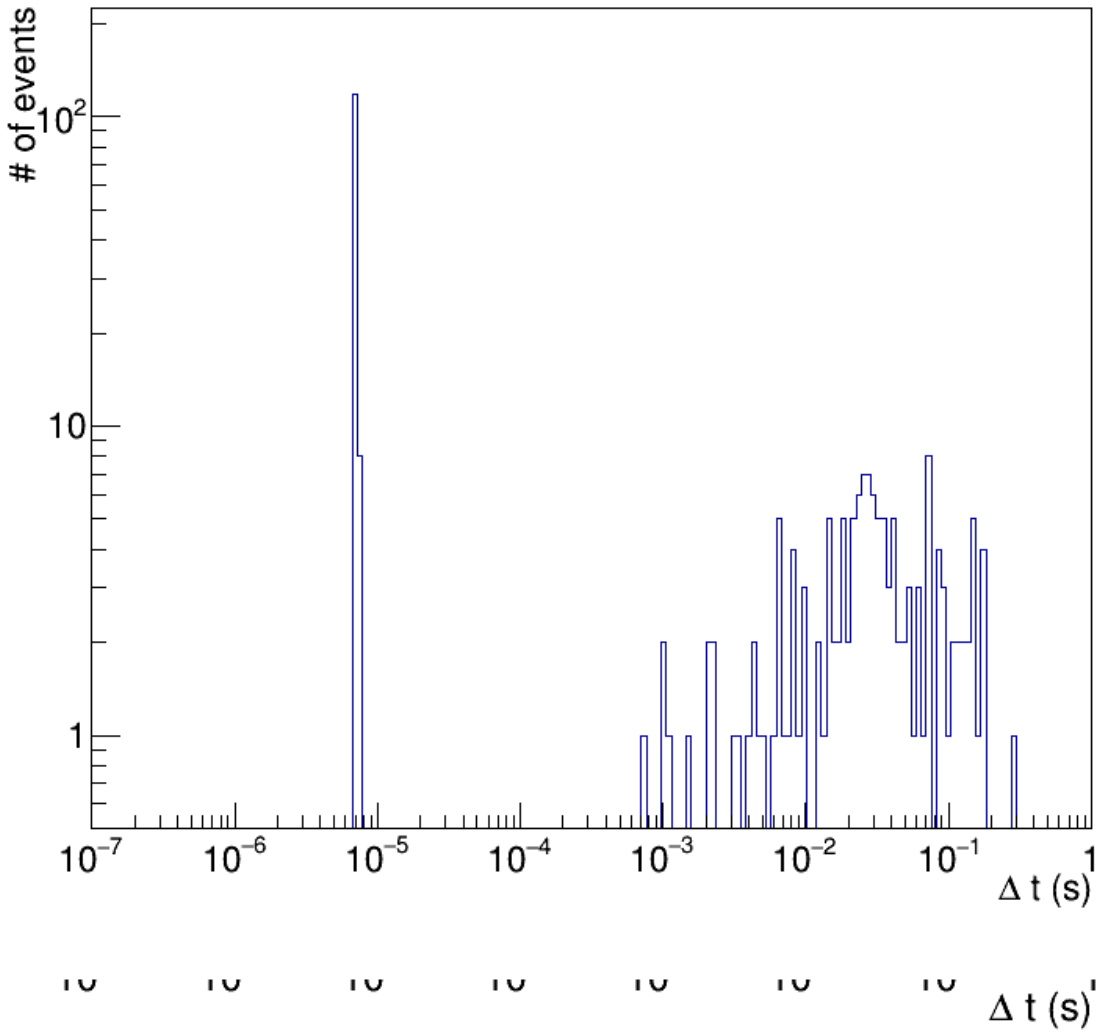

Figure 6.10: *Time differences, dt defined in text, for HiCal pointed events in run 413. The only events having a Δt within the dt given in the text are confirmed to be paired HiCal events indicating that HiCal events are not missing in the ANITA dataset due to interfering events.*

6.2.2 ANITA Efficiency From WAIS Ground Pulser

For the ANITA-3 flight, ground pulsers were deployed at the West Antarctic Ice Sheet (WAIS) remote station and at the Long Duration Balloon (LDB) launch site. We will use the ANITA efficiency for recording events from the WAIS pulser and apply this efficiency to the HiCal event distribution, then determine if the adjusted distribution of HiCal events has shifted lower, in terms of peak amplitude, to the point that would indicate a significant number of reflected events would have occurred with amplitudes below the ANITA trigger threshold. Generally, the ANITA efficiency is measured using ground pulser events as a function of the detected event amplitude or power (peak voltage, peak Hilbert envelope, or SNR). For use with the HiCal events, since we specifically want a way to account for ANITA dead-time, we will instead use a 2D efficiency based on peak voltage and per second event rate.

To determine this efficiency, all events that occurred while the WAIS pulser was on were used. The WAIS pulser transmitted a pulse once per second latched to a specific sub-second. WAIS events are identified using this sub-second and the TOF from the ground station to ANITA. Figure 6.11 shows the efficiency as a function of peak waveform voltage and the per-second event rate of the second corresponding to the recorded event.

6.2.3 Applying Efficiencies to Detected Events

Figure 6.12 shows examples from two runs for the peak voltage distributions before and after adjusting them based on the WAIS efficiencies. The adjustments were made to the HiCal events on an event by event basis, according to the same measures used to make the WAIS efficiency plot: peak amplitude of the event waveform and per-second event rate during the second in which the event occurred. These example runs show two different cases, one in which the adjusted distributions would not indicate a significant number of missing reflected events (the bottom set of plots in the figure) and one which would (the top set of plots in the figure).

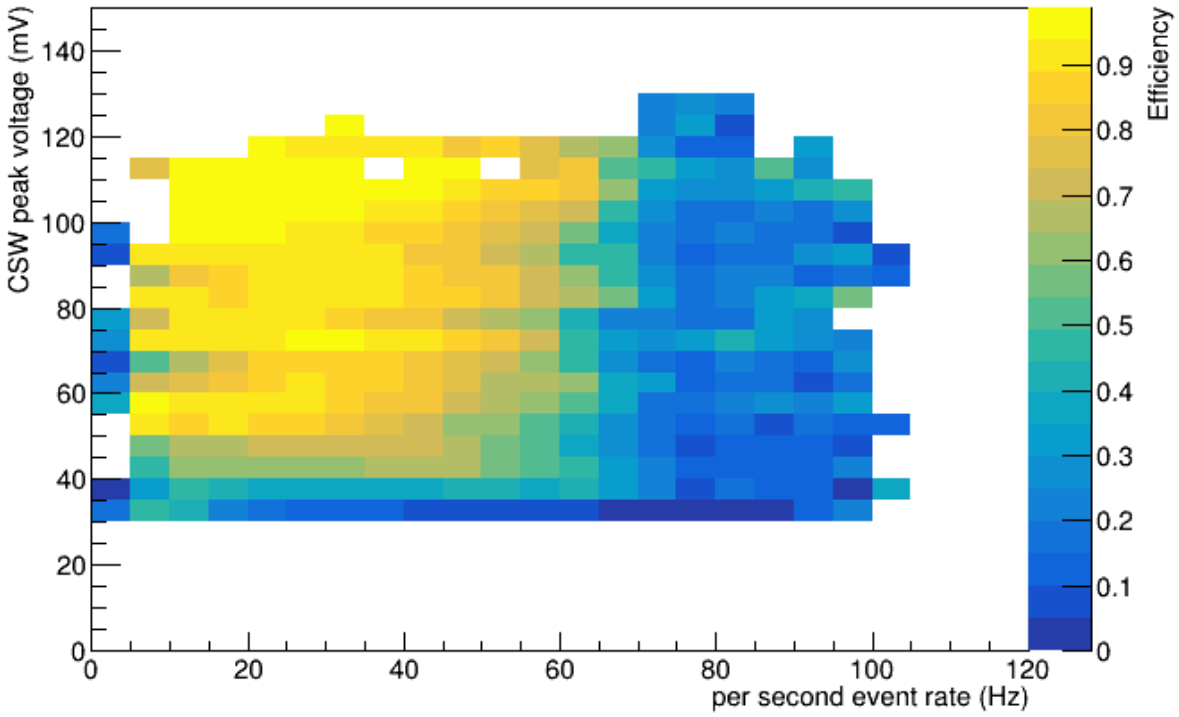

Figure 6.11: *Efficiency of detection of WAIS ground pulser events as a function of peak waveform voltage and the per-second event rate of the second corresponding the the recorded event.*

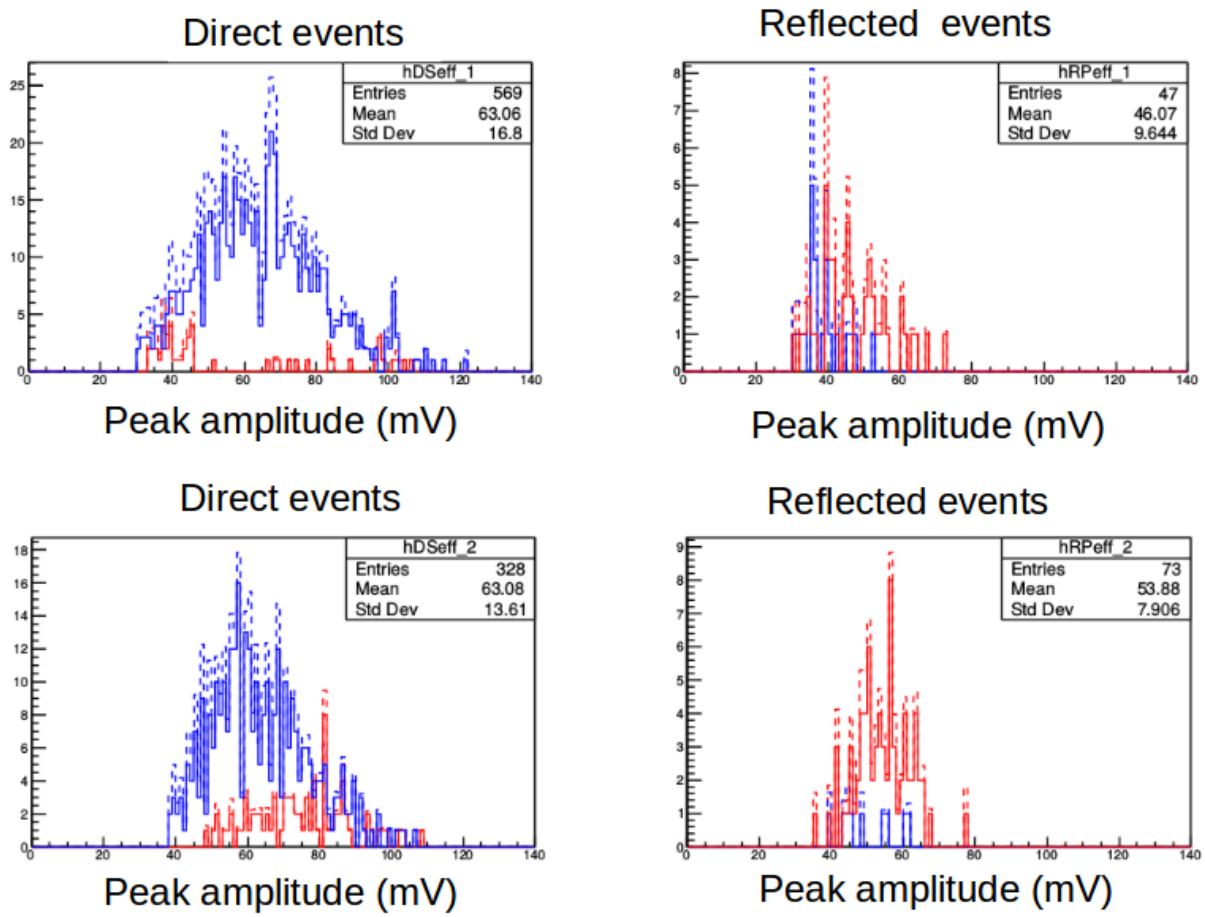

Figure 6.12: *Peak amplitude distributions for direct (left plots) and reflected (right plots) events for two runs. The blue lines indicate single, unpaired events and the red lines indicate paired events in all plots. The solid lines are the detected events and the dotted lines are the efficiency adjusted distributions.*

6.3 Reflection Coefficients from HiCal Events

Figure 6.13 shows the amplitude ratios for paired reflected and direct events for the entirety of the HiCal-1b flight. These ratios are taken from the peak amplitudes of the CSW and unadjusted. The most significant issue with these values is that some of the ratios have a value >1, which would only be possible if there is a surface effect that is boosting the reflected amplitude or if the HiCal transmitter gain is greater in the direction of the reflected path compared to the direct. For the latter possibility, Figure 6.14 shows the azimuth dependent transmitter gains in the direct and reflected directions for a typical separation angle. Since the ANITA and HiCal payload separation distances were large, the direct -to-reflected separation angle from the transmitter were small and the difference in gains is not sufficient to explain the larger-than-anticipated reflection ratios.

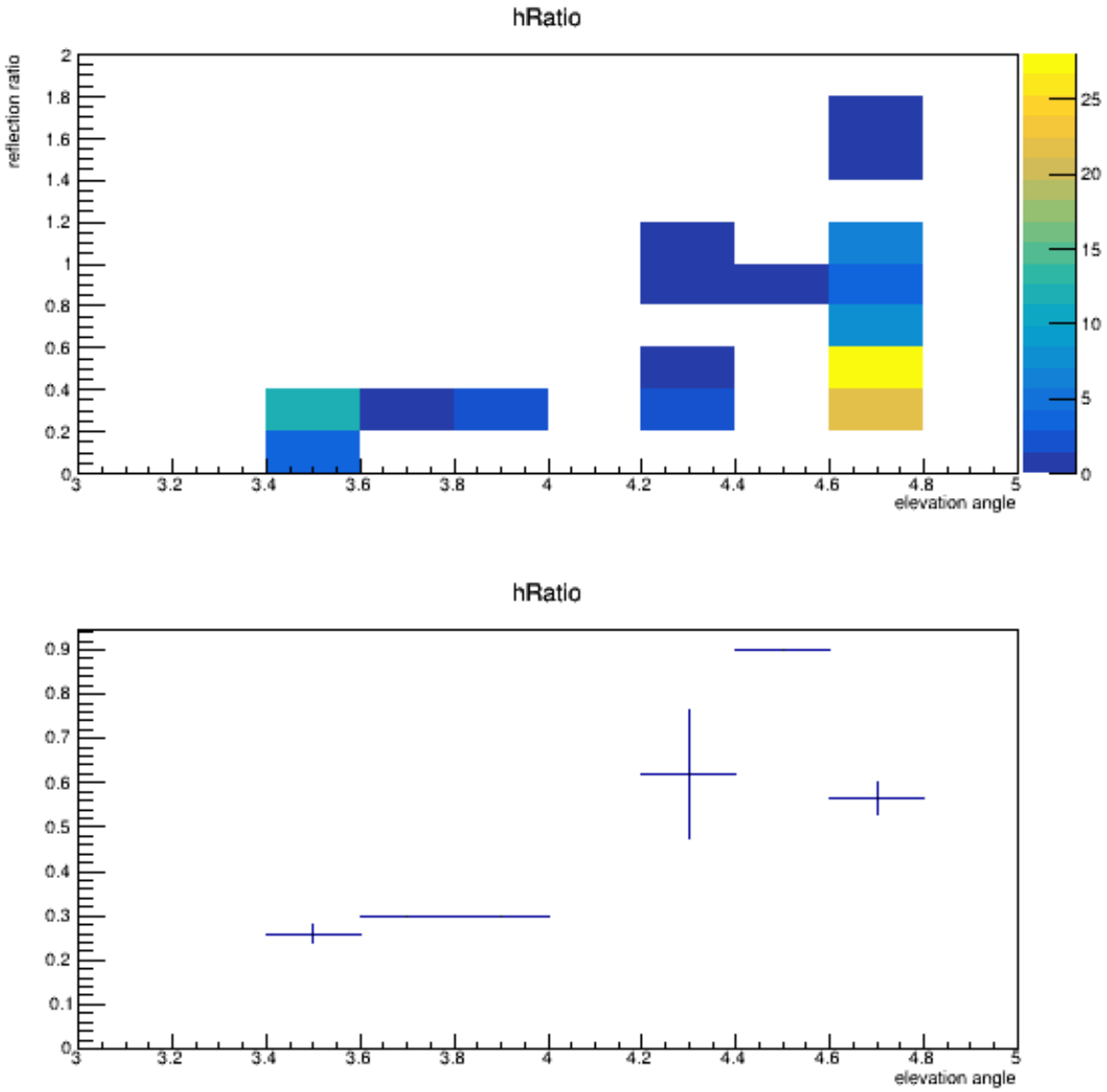

Figure 6.13: *Waveform amplitude reflection ratios for the entirety of the HiCal-1b flight. The top plot shows the values binned in elevation angle and ratio value with the color axis showing number of events in each bin, while the bottom plot shows the averaged values for each elevation angle bin.*

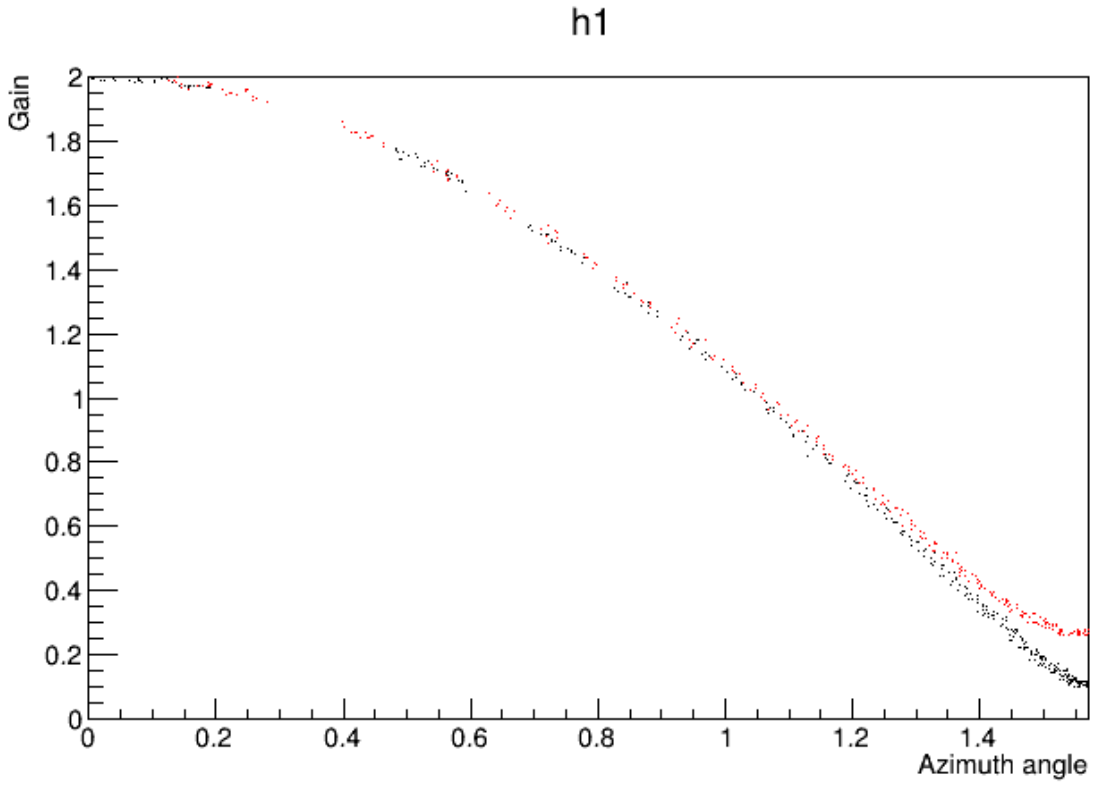

Figure 6.14: *HiCal transmitter gain pattern for one quadrant of azimuth angle at two elevation angles representing the direct signal direction (black) and the reflected signal direction (red). Angle is in radians and gain is in dB.*

Chapter 7

Conclusions

7.1 Analysis Summary

The HiCal experiment was designed to measure the Antarctic surface reflectivity at oblique incidence angles in the range where CR detection by ANITA is expected and has been demonstrated. The reflectivity results from HiCal-1, re-binned from Figure 6.13, are shown in Figure 7.1 along with results from the ANITA-2 and ANITA-3 solar reflectivity analysis, the more recently completed HiCal-2 analysis, and three theoretical curves based on the modeling methods discussed in Chapter 4. We note reasonable agreement between the HiCal-1 data and the lowest elevation angle data from HiCal-2. Although the Solar measurements give good consistency with 'raw' Fresnel, the HiCal measurements show a clear deficiency of signal relative to the expectation from the Fresnel equations at elevation angles $< 5^{\circ}$. At these elevation angles, equivalent to very glancing incidence angles, the HiCal measurements indicate important surface-decoherence effects. If correct, our results imply that the estimates of cosmic ray energies from the ANITA experiment over-corrected for surface reflectivity. In that case, the average CR energy measured by ANITA is actually lower than previously inferred, which increases the discrepancy between the ANITA CR flux measurement relative to other experiments measuring the UHECR cosmic ray spectrum. Going forward, the surface reflection measurements from this work should be included in the re-

construction of events from the ANITA data.

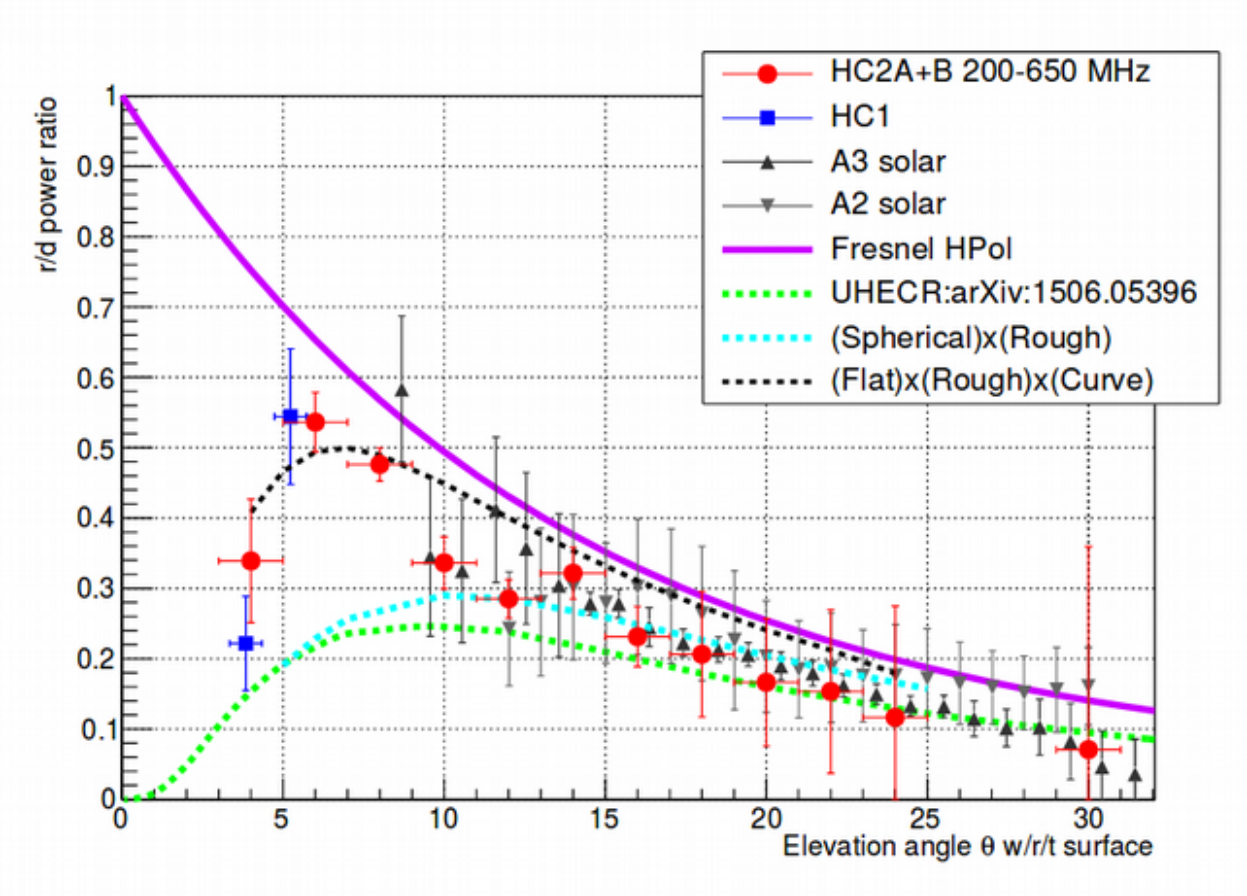

Figure 7.1: *Summary of all reflectivity results from ANITA data analysis including the solar reflection analysis from ANITA-2 and ANITA-3 and the more recently completed results from HiCal-2 flown with ANITA-4. The solid line shows the predicted Fresnel reflection coefficients and the dotted lines show various theoretical preditictions for the reflection coefficients taking into account different combinations of effects including earth curvature and roughness. The HiCal-1 results included are rebinned from the same data shown in Figure 6.13. Figure from [40].*

.

7.2 Outlook and Future Work

Thus far, we have collected reflectivity data using the solar reflection and HiCal transmitted signals. Both sets of data cover a wide range of reflection incidence angles. The solar data also covers a wide range of geographical locations. However, there is not significant overlap in the surface locations between the solar reflections and HiCal reflections which limits our ability to extrapolate

the results of the HiCal data across a greater area of the continent for location specific reflectivities. Also, only the solar data provided measurements in the vertical polarization which has greater relevance to neutrino detection as signals from these events would be transmitted through the air-ice interface in the vertical polarization.

At minimum, any future HiCal flight should 1) produce triggered pulses tied to the GPS second to aid in identifying the events in the ANITA data sample, 2) include payload azimuth angle orientation monitoring to provide direct measurements of antenna beam pattern for event analysis, and 3) have power provided from solar panels to extend the lifetime of the payload. Additional desired features would be to 1) develop an on-board DAQ and use the antenna to transmit and receive normal incidence reflection signals and 2) equip the payload with multiple antennas or a dual polarized antenna to produce signals in the HPol and VPol. Furthermore, HiCal missions independent of ANITA flights could be accomplished using pairs or multiple HiCal payloads on individual balloons. There is also the potential to fly a HiCal transmitter on a satellite mission, which, if timed to coincide with ANITA-5, could greatly increase the surface area coverage of collected data and also provide cross-experiment calibration pulses between ANITA and the other ground based neutrino experiments in Antarctica.

References

[1] Victor Hess. *Physikalische Zeitschrift*, 13, 1912.

[2] A. Widom, J. Swain, and R. Srivastava. Bremsstrahlung energy losses for cosmic ray electrons and positrons. *arXiv:1509.08365 [hep-ph]*, 2015.

[3] R. Ruffini, G.V. Vereshchagin, and SS. Xue. *Astrophys Space Sci*, 361:82, 2016.

[4] Francis Halzen. High-energy neutrino astronomy: the cosmic ray connection. *Reports on Progress in Physics*, 65(7):1025–1078, 2002.

[5] A. Romero-Wolf and M. Ave. Bayesian inference constraints on astrophysical production of ultra-high energy cosmic rays and cosmogenic neutrino flux predictions. *J. of Cosmology and Astroparticle Physics*, 2018(07):025, 2018. URL `http://stacks.iop.org/1475-7516/2018/i=07/a=025`.

[6] M. Ahlers. High-energy cosmogenic neutrinos. *Physics Procedia*, 61:392 – 398, 2015. ISSN 1875-3892. doi: https://doi.org/10.1016/j.phpro.2014.12.080. URL `http://www.sciencedirect.com/science/article/pii/S1875389214006932`. 13th International Conference on Topics in Astroparticle and Underground Physics, TAUP 2013.

[7] K. Kotera. Cosmogenic neutrinos: arameter space and detectabilty from pev to zev. *J. of Cosmology and Astroparticle Physics*, 2010(10):013–013, 2010.

[8] S. Hussain and D.W. McKay. Comparative study of radio pulses from simulated hadron-,

electron-, and neutrino-initiated showers in ice in the gev-pev range. *Phys. Rev. D*, 70(10), 2004.

[9] J. Jones et al. Tracing very high energy tau neutrinos from cosmological distances in ice. *Int. J. Mod. Phys.*, 20(6):1204–1211, 2004.

[10] ANITA Collaboration: P. Gorham et al. Observations of the askaryan effect in ice. *Physical Review Letters*, 99(17), 2007.

[11] P. Gorham et al. Measurements of the suitability of large rock salt formations for radio detection of high-energy neutrinos. *Nuclear Inst. and Methods in Physics Research, A*, 490 (3):476–491, 2002.

[12] D. Williams. *The Askar'yan effect and detection of extremely high energy neutrinos in the lunar regolith and salt*. PhD thesis, 2004.

[13] R. Milincic. *Measurements of Askaryan effect in salt*. PhD thesis, 2006.

[14] P. Gorham et al. Radio-frequency measurements of coherent transition and cherenkov radiation: Implications for high-energy neutrino detection. *Physical Review E*, 62(6), 2000.

[15] P. Miocinovic. Tuning into uhe neutrinos in antarctica - the anita experiment. *arXiv.org*, 2005.

[16] A. Silvestri for the ANITA Collaboration. Status of anita and anita-lite. *arXiv:astro-ph/0411007*, 2004.

[17] J. Nam et al. Preliminary result from anita experiment. *Modern Physics Letters A*, 23(17-20): 1419–1430, 2008. ISSN 0217-7323.

[18] Dave Besson. Radio cherenkov detection of neutrinos. *Nuclear Instruments and Methods in Physics Research Section A: Accelerators, Spectrometers, Detectors and Associated Equipment*, 588(1):138 – 145, 2008. ISSN 0168-9002. doi: https://doi.org/10.

1016/j.nima.2008.01.029. URL http://www.sciencedirect.com/science/article/pii/S0168900208000557. Proceedings of the First International Conference on Astroparticle Physics.

[19] P. Gorham et al. The antarctic impulsive transient antenna ultra-high energy neutrino detector: Design, performance, and sensitivity for the 2006–2007 balloon flight. *Astroparticle Physics*, 32(1):10–41, 2009. ISSN 0927-6505.

[20] P. Gorham et al. Observational constraints on the ultrahigh energy cosmic neutrino flux from the second flight of the anita experiment. *Physical Review D*, 82(2), 2010. ISSN 1550-7998.

[21] A. Connolly. Anita status. *Nuclear Inst. and Methods in Physics Research, A*, 604(1):S98–S101, 2009. ISSN 0168-9002.

[22] P. Gorham. Constraints on the diffuse high-energy neutrino flux from the third flight of anita. *Phys. Rev. D*, 98:022001, Jul 2018. doi: 10.1103/PhysRevD.98.022001. URL https://link.aps.org/doi/10.1103/PhysRevD.98.022001.

[23] P. Gorham et al. Characteristics of four upward-pointing cosmic-ray-like events observed with anita. *Phys. Rev. Lett.*, 117:071101, Aug 2016. doi: 10.1103/PhysRevLett.117.071101. URL https://link.aps.org/doi/10.1103/PhysRevLett.117.071101.

[24] P. Gorham et al. Observation of an unusual upward-going cosmic-ray-like event in the third flight of anita. *Phys. Rev. Lett.*, 121:161102, Oct 2018. doi: 10.1103/PhysRevLett.121.161102. URL https://link.aps.org/doi/10.1103/PhysRevLett.121.161102.

[25] D. Besson. In situ radioglaciological measurements near taylor dome, antarctica and implications for ultra-high energy (uhe) neutrino astronomy. *Astroparticle Physics*, 29(2):130–157, 2008.

[26] D. Besson, R. Keast, and R. Velasco. In situ and laboratory studies of radiofrequency prop-

agation through ice and implications for siting a large-scale antarctic neutrino detector. *Astroparticle Physics*, 31(5):348–358, 2009.

[27] M. Stockham. PhD thesis, 2018.

[28] B.W. Carroll and D.A. Ostlie. *An Introduction to Modern Astrophysics*. Cambridge University Press, 2007.

[29] A. M. Hillas. The origin of ultra-high-energy cosmic rays. *Annual Review of Astronomy and Astrophysics*, 22, 1984.

[30] F. Schroder. Radio detection of cosmic-ray air showers and high-energy neutrinos. *Progress in Particle and Nuclear Physics*, 93:1–68, 2017.

[31] T. Huege. Radio detection of cosmic ray air showers in the digital era. *Physics Reports*, 620: 1–52, 2016.

[32] D. Saltzberg et al. Observation of the askaryan effect: Coherent microwave cherenkov emission from charge asymmetry in high-energy particle cascades. *Phys. Rev. Lett.*, 86:2802–2805, Mar 2001. doi: 10.1103/PhysRevLett.86.2802. URL `http://link.aps.org/doi/10.1103/PhysRevLett.86.2802`.

[33] I. Kravchenko et al. Updated results from the rice experiment and future prospects for ultra-high energy neutrino detection at the south pole. *Phys. Rev. D*, 85:062004, Mar 2012. doi: 10.1103/PhysRevD.85.062004. URL `https://link.aps.org/doi/10.1103/PhysRevD.85.062004`.

[34] P. Allison et al. Performance of two askaryan radio array stations and first results in the search for ultrahigh energy neutrinos. *Phys. Rev. D*, 93:082003, Apr 2016. doi: 10.1103/PhysRevD.93.082003. URL `https://link.aps.org/doi/10.1103/PhysRevD.93.082003`.

[35] S.W. Barwick et al. A first search for cosmogenic neutrinos with the arianna hexagonal radio array. *Astroparticle Physics*, 70:12–26, 2015. ISSN 0927-6505. doi: https://doi.org/

10.1016/j.astropartphys.2015.04.002. URL http://www.sciencedirect.com/science/article/pii/S0927650515000638.

[36] A. Romero-Wolf et. al. An interferometric analysis method for radio impulses from ultra-high energy particle showers. *Astroparticle Physics*, 60:72–85, 2015.

[37] H. Schoorlemmer et al. Energy and flux measurements of ultra-high energy cosmic rays observed during the first anita flight. *Astroparticle Physics*, 77:32–43, 2016.

[38] S.G Warren, R. E. Brandt, and P.O. Hinton. Effect of surface roughness on bidirectional reflectance of antarctic snow. *J. Geophys. Res.*, 103:25,789–25,807.

[39] A. Romero-Wolf et al. Concept and analysis of a satellite for space-based radio detection of ultra-high energy cosmic rays. *American Astronomical Society Meeting Abstracts*, 223 (211.01), 2013. arXiv: 1302.126.

[40] S. Prohira et al. Antarctic surface reflectivity calculations and measurements from the anita-4 and hical-2 experiments. *arXiv:1801.08909v1 [astro-ph.IM]*, 2018.

[41] M.K. Shepard, R.A. Brackett, and R.E. Arvidson. Self-affine (fractal) topography: Surface parameterization and radar scattering. *J. of Geophys. Res.*, 100:11,709–11,718, 1995.

[42] M.K. Shepard and B.A. Campbell. Radar scattering from a self-affine fractal surface: Near-nadir regime. *Icarus*, 141:156–171, 1999.

[43] M. Sylvain. Diffuse reflection by rough surfaces: an introduction. *C. R. Physique 6 663–6743*, 2005.

[44] SP Neeck, TJ Magner, and GE Paules. Nasa's small satellite missions for earth observation. *Acta Astronautica*, 56(1):187–192, 2005.

[45] PA Dubock et al. The envisat satellite and its integration. *ESA bulletin*, 106:26–45, 2001.

[46] P.W. Gorham et al. Antarctic surface reflectivity measurements from the anita-3 and hical-1 experiments. *Journal of Astronomical Instrumentation*, 06(02):1740002, 2017. doi: 10.1142/S2251171717400025. URL https://www.worldscientific.com/doi/abs/10.1142/S2251171717400025.

[47] D. Z. Besson et al. Antarctic radio frequency albedo and implications for cosmic ray reconstruction. *Radio Science*, 50(1):1–17, 2015. ISSN 1944-799X. doi: 10.1002/2013RS005315. URL http://dx.doi.org/10.1002/2013RS005315. 2013RS005315.

[48] H. Liu, K. C. Jezek, B. Li, and Z. Zhao. Radarsat antarctic mapping project digital elevation model, version 2, 2015. doi: https://doi.org/10.5067/8JKNEW6BFRVD.